Plasma Assisted Surface Atomic Layer Substitution

For Creating Janus 2D Materials

By

Dipesh Trivedi

A Thesis Presented in Partial Fulfillment
of the Requirements for the Degree
Master of Science

Approved July 2019 by the
Graduate Supervisory Committee:

Sefaattin Tongay, Chair
Matthew Green
Houlong Zhuang

ARIZONA STATE UNIVERSITY

August 2019

ABSTRACT

More recently there have been a tremendous advancement in theoretical studies showing remarkable properties that could be exploited from transition metal dichalcogenide (TMDC) Janus crystals through various applications. These Janus crystals are having a proven intrinsic electrical field due to breaking of out-of-plane inversion symmetry in a conventional TMDC when one of the chalcogenides atomic layer is being completely replaced by a layer of different chalcogen element. However, due to lack of accurate processing control at nanometer scales, key for creating a highly crystalline Janus structure has not yet been familiarized. Thus, experimental characterization and implication of these Janus crystals are still in a state of stagnation. This work presents a new advanced methodology that could prove to be highly efficient and effective for selective replacement of top layer atomic sites at room temperature conditions.

This is specifically more focused on proving an easy repeatability for replacement of top atomic layer chalcogenide from a parent structure of already grown TMDC monolayer (*via* CVD) by a post plasma processing technique. Though this developed technique is not limited to only chalcogen atom replacement but can be extended to any type of surface functionalization requirements.

Basic characterization has been performed on the Janus crystal of SeMoS and SeWS where, creation and characterization of SeWS has been done for the very first time, evidencing a repeatable nature of the developed methodology.

I dedicate this work to my mother, father, grandparents and my entire extended family. Without their love and support, it would have been very difficult for me to achieve this platform.

ACKNOWLEDGMENTS

I would like to express my profound sense of gratitude to my advisor and mentor, Dr. Sefaattin Tongay, for allowing me to be a part of his group and letting me work by utilizing the full potential of the facilities he maintains. His immense knowledge in the field of 2 dimensional materials has helped me through my journey as a master's student. I cannot think of a better advisor with such a strategic guidance and enthusiasm towards every project I was involved at Arizona State University.

I am also thankful to all the group members for their much-needed ideologies and unceasing assistance on my projects, specially Dr. Guven. Not only were you supportive in my research but you also made this journey extremely enjoyable with an extreme sense of humor.

A ward of thanks to various collaborators from ASU and beyond, for their contribution to my research and for providing me with eloquent results that supported my conclusions more effectively. Special thanks to Dr. Houlong Zhuang and team for all their assistance.

Last but not the least, I am indebted to my parents who have always supported me morally and backed me through difficult times.

TABLE OF CONTENTS

Page

CHAPTER Page

CHAPTER Page

LIST OF TABLES

LIST OF FIGURES

Figure Page

Figure Page

Figure Page

Chapter 1 Introduction

1.1 2D layered materials

Since the dawn of civilization, every age has been defined by the predominant material it used, from the stone ages, about 3.4 million years ago up to the onset of the silicon age with the birth of the transistor in 1947[1], materials have been the hallmark of a civilizations' progress. With the rediscovery and isolation of graphene in 2004 [2][3], many speculated the beginning of what is now called the carbon age. Projected as a wonder material, Graphene became a sensation amongst the materials community, due to its fascinating properties. Its strong ambipolar electric field effect and high room temperature mobility made it a suitable candidate for metallic transistor applications [2]. The following decade saw extensive research to understand its optical, physical and electrical characteristics. Owing to its excellent mechanical flexibility and durability, graphene was soon seen as structural enhancement material and it was employed as a constituent in composite materials [4][3][5]. Its extraordinary optical transparency, superb carrier mobility and remarkable stability also led researchers to speculate its use in electronics [6][7].

Yet despite these advantages, it failed to cement its place within the semiconductor industry. This was mainly due to the lack of an electronic bandgap; researchers, however, were soon able to overcome this drawback by asymmetric functionalization and decoration of graphene molecules[7]. Bandgap modulation hence was then a possibility and was predicted in the form of decorating graphene to "graphane" via hydrogen on both sides, this allowed for the widening of the band gap from zero to 3.7 eV [8]. A couple of years later, researchers reported an asymmetrically functionalized version of graphene called "graphone" which was an indirect bandgap ferromagnetic semiconductor [9].

Similar studies were carried out by decorating graphene with halogens and they showed substantial promise for bandgap modulation [10]. These theoretical studies showed the tremendous potential to modify this remarkable material to tailor the needs of the 21st century. Another aspect of graphene was that it also opened new avenues for research into similar kinds of materials. The "two-dimensional material", an umbrella term to categorize graphane like materials, emerged a few years after the graphene was synthesized. Under these, The Transition Metal Dichalcogenides (TMDC) is perhaps the most well-known and much thoroughly researched. The research TMDC materials spiked after the discovery of strong photoluminescence in MoS2 monolayers, a TMDC showing direct bandgap in atomically thin monolayer[11], [12].

The first reports on the structure of the TMDCs date back to Pauling in 1923 and since then more than 60 different types of TMDC's have been theorized, with over 40 of them showing a layered structure[13]. Yet it was after Giem and Novoselov discovery that this class of materials was researched upon with renewed interest. Since then MoS2 has been the flagship of TMDC materials and it has gained most attention of the scientific community, since the past decade was devoted to synthesis and study of graphene, the methodology and the early research routes were quite well-established to be applied to these classes of materials, and just like graphene these materials also promised to show wide range of electronic properties, atomically thin structure, tunable bandgap, and a potential for a wide range of applications in optoelectronic, spintronics and low power electronics [14]. Report of synthesis of monolayer MoS2 dates to 1963, however thanks to the research and development on CVD growth of graphene in the latter half of the decade, rapid, high-quality synthesis of monolayer TMDC's was possible.

1.2 Transition Metal Dichalcogenides

1.2.1 MoS2

A naturally occurring layered material with strong in-plane bonding and weak out of plane interaction, MoS2 is perhaps the most well-known example of a TMDC material, it is by far the most extensively research and studied material in this category. Bulk MoS2 is a diamagnetic, indirect bandgap semiconductor [11]. Earliest sources of monolayer MoS2 dates to back to Frindt in the early sixties, who isolated the monolayer by using mechanical exfoliation in the late eighties [15][16], and up until the late 2000s majority of these monolayers were used as substrates for characterization and study of organic macromolecules by STM [17]–[21]. Emergence of graphene enabled the search for atomically thin materials with semi-conducting nature, in light of this, studies with MoS2 as a possible 2D direct band semiconductor was proposed in 2010 [11], [12].

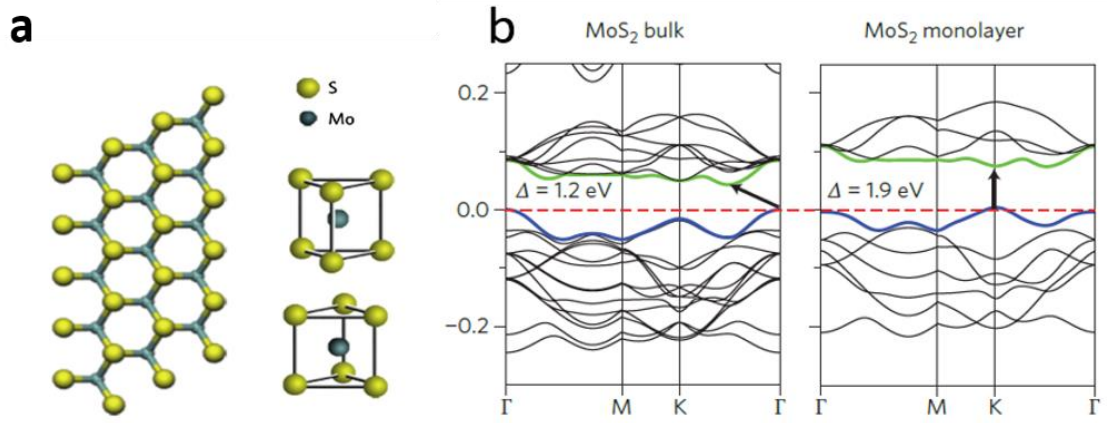

Figure 1.1 (a) MoS2 crystal structure (b) Phonon dispersion of bulk and monolayer MoS2 [67]

High-quality monolayer MoS2 can be reliably grown using techniques such as MBE (Molecular Beam Epitaxy) and CVD (Chemical Vapor Deposition). Highly crystalline monolayers of MoS2 with thickness up to 120 μm sizes have been reported using CVD with

flakes showing superior optical and electrical properties when compared to their exfoliated counterpart [22]. Unlike the bulk crystal, monolayer MoS2 is direct bandgap semiconductor with a stable 2H phase. MoS2 shows valley dependent physical phenomena due to inequivalent high symmetry points along the corners of the Brillouin zone which has led to speculation of potential valleytronics applications. Due to the lack of in-plane inversion symmetry, monolayer 2H-MoS2 shows the spin splitting of the electronic bands via spin-orbit interaction, this spin-valley coupling can be used to design spintronic devices and potential spintronic applications [23], [24]. Theoretical prediction of monolayer MoS2 have shown the electron transport mobility in the range of 10-1000 $cm^2/(V\text{-}s)$ and low-temperature values ranging and exceeding 1000 $cm^2/(V\text{-}s)$ [25]. Thus as one of the flagship materials of the TMDC classes of materials, researchers have predicted a plethora of application for MoS2 and similar class of materials due to their many interesting properties and rich physics [14].

1.2.2 Janus TMDC

Asymmetric functionalization of the TMDC monolayer gathered widespread attention in the early half of this decade. Aptly named “Janus” after the Roman god of beginnings and ends, this term has been used to denote a wide selection of materials that show different properties on two opposing faces or sides. These materials gained popularity after atomic modification of monolayer graphene had led to widening of its bandgap and thus allowed for band engineering opportunities in atomically thin materials [26], [27]. A wide number of DFT-based studies have predicted these materials to be useful for several applications [10], [28]–[34]. While Janus class of materials is an umbrella term loosely applied to asymmetrically functionalized macromolecules, what distinguishes TMDC-based Janus materials with others is the functionalization in atomically thin

monolayers that can be suited to innumerable applications within the electronics industry. Another important distinction that must made about these materials is mainly related to their structures and how they differ from TMDC alloys.

1.2.3 Structural differences from conventional TMDC alloys

A materials property is mainly dictated by its symmetry, and while symmetric materials have been extremely functional, it is the breaking of the symmetry in these Janus TMDC that make things interesting. The disturbance of symmetry within these materials leads to interesting phenomena, such as phase transition, ferroelectricity and ferromagnetism [35]–[40]. Traditionally the idea of breaking the symmetry within these materials arrived through graphene, a necessity in order to overcome zero bandgap [7] [8]. Another method to do so was via the creation of van der Waals heterostructures, by stacking sheets of these materials on top of other.

Yet development and creation van der Waals heterostructure at a commercial scale is still an immature field and will require thorough research to realize them practically. Synthesis of Janus however enables this in a rather more efficient fashion and the proposal of the first polar TMDC monolayer provided important guidance for future experimental studies [41]. Janus materials based on the group-III and group-VI chalcogenides have been extensively investigated [42], [43]. Unlike the MoS2 monolayer with a D_{3v} symmetry, Janus group-VI chalcogenides have a C_{3v} symmetry, this is observed due to the breaking of mirror symmetry after the functionalization of its top layer. This results in a non-uniform charge distribution owing to the difference in the atomic radii and the electronegativity.

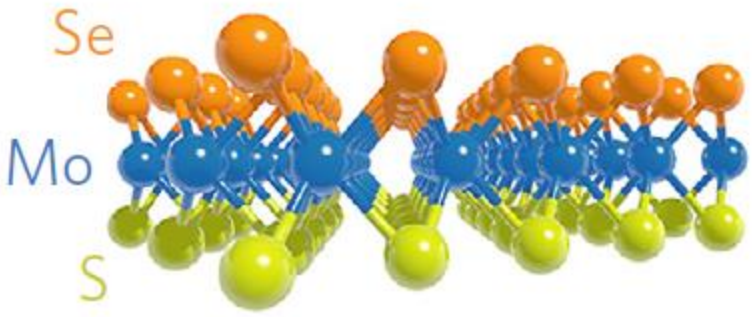

Figure 1.2 Janus structure of SMoSe TMDC [65]

Janus TMDCs are a new emerging class of materials that have been predicted to show Rashba type splitting. Due to the absence of mirror symmetry, materials with a large Rashba spin splitting are promising candidates for spintronic applications. DFT based calculation on phonon dispersion and the dynamic stability of these monolayers have shown them to be stable[26], [44], [45]. Recently the group-III based Janus chalcogenides have also been studied and predicted to be stable according to the formation energy and phonon dispersion calculations [46]

1.3 Applications

Electronic structure is quite important in predicting the physical properties of materials. Studies on the band structures of 2D TMDC materials and their derivatives have been carried out in detail. When synthesized as a monolayer, the band structure in most TMDC's changes, from indirect in bulk to direct in monolayers [11]. TMDC monolayers with suitable, tunable, and direct bandgaps provide a high optical absorption coefficient for photovoltaic devices. The group-III chalcogenide Janus monolayers are shown to be semiconducting, with an indirect bandgap of 1.32–2.36 eV. The high carrier mobility indicates that TMDCs are suitable for use in electronic devices, such as field-effect transistors [44].

A momentum dependent spin splitting of spin band within two dimensional systems, the Rashba effect induces various novel physical phenomena and is important in spintronics [55]. Over the years, researchers have carried out many studies in order to realize the Rashba effect within a variety of class of Janus materials [37], [38], [55]–[60]. After the synthesis of Janus MoSSe, researchers soon began to investigate electronic band structures of a series of Janus monolayer TMDCs with chemical formula MXY. A Rashba-type spin splitting around the gamma point has been predicted for all the MXY systems [56]. The spin splitting can be enhanced by an external electric field collinear with the local electric field derived by the polar bonds and by the compressive strain. Considering the spin–orbit coupling, the band structures of the Janus MXY monolayers show strong spin splitting at band edges around the K-point, which is similar to MX2 monolayers [40], thus showing a potential for applications in spintronic devices. Like the traditional MX2, the bandgap of MoSSe increases with a decrease in thickness due to the quantum confinement effect [11], [26].

Recent studies in the functionalization of Janus TMDC namely MoSSe nanotubes has been predicted to be one of the forerunners for photocatalytic application[53]. Janus MXenes have also been theoretically been predicted to show a lot of promise for photocatalysis [26], [47]–[49], [52], [54].

Piezoelectricity in 2D van der Waals materials has also received considerable interest because of potential applications in nanoscale energy harvesting, sensors, and actuators [58]. Because of the absence of mirror symmetry, a large in-plane and normal piezoelectric effect can be realized in the monolayers and multilayers of Janus 2D TMDCs. Janus structures for piezoelectric materials starting from group-III monochalcogenide are predicted to be having thermodynamically stable monolayers [63]. For MXY monolayers,

both strong in-plane and much weaker out-of-plane piezoelectric polarizations can be induced by a uniaxial strain in the basal plane [64].

More recently, H type Janus-VSSe has been shown to be more stable than the T type, and dynamically stable through phonon frequency analysis. The results predicted H type Janus-VSSe as a magnetic semiconductor exhibiting values of in-plane piezoelectricity, the in plane and vertical piezoelectricity for these magnetic materials are higher than traditional 3D piezoelectric materials such as α-quartz [36]. In multilayer MXY, a very strong out-of-plane piezoelectric polarization was obtained when the out-of-plane piezoelectric coefficient was found to be strongest in multilayer MoSTe [64]. Perhaps the most promising of these is the prediction of room-temperature ferromagnetic Janus monolayer VSSe which showed large valley polarization due to the broken space- and time-reversal symmetry.

1.4 Janus Experimentation review

In the year 2017, the first experimental realization of these Janus based materials were realized in the form of MoSSe independently [65], [66] Although the ability to duplicate the results predicted in the 2017 study to other class of similar materials should have attracted much attention, nevertheless no Janus forms of materials have been presented or developed. The reason for such a discrepancy might be associated with the still immature understanding of these materials and their synthesis. Lu et. al, one of the two groups who synthesized Janus MoSSe relied on the surface decoration of CVD grown MoS2 via an in-situ selenization process. This process relied on stripping of the top layer of the MoS2 monolayer under the influence of ionized plasma generated via an inductively coupled plasma setup. This is followed by a second step of thermal selenization in which the recently stripped off top layer is replaced by the now thermally activated selenium ions.

The entire process was carried out at lower pressure within a vacuum tube to avoid contamination via atmosphere. The process was especially important in establishing the synthesis of Janus MoSSe or any such class of molecules was heavily implied on by the control of the reaction kinetics. In the same year, Zhang et al. and the research group co-independently also synthesized Janus MoSSe via an in-situ sulfurization process. Starting out with $MoSe_2$ based CVD materials, the top layer was sulfurized within a tube at 800°C temperatures at 1 atm pressures. Both studies characterized and confirmed the existence of these materials via a series of characterization tests such as XPS and STEM. The results from the two studies correlated well the theoretical predictions [65], [66].

Chapter 2 Synthesis and characterization process

It's been two years since any of these materials have been functionalized or studied again. Part of the reason for this is the poor repeatability of the initial studies and lack of fundamental understanding of these materials, considering this, efforts have been made to establish a first standard operating procedure and a process to synthesize superior class Janus based materials at room temperature. The results of the synthesis corelated well with the previous studies, and synthesis protocol can be easily extended to other class of materials without much modification. This section will be focused on understanding some of the tools and techniques used for growing and characterizing Janus crystals.

2.1 Top down approach

There are various top down approaches that could be incorporated for synthesizing bulk crystals which is then followed by exfoliation technique to get to monolayers thick films. But here, only one of those technique will be discussed in brief namely chemical vapor transport (CVT).

2.1.1 CVT followed by exfoliation

Chemical Vapor Transport (CVT) is a very basic technique for growing good quality bulk crystals which relies majorly on the thermodynamics of a system. As the name suggests, in this process a material in solid phase is sublimed and transported in crystal form from a hot zone to a colder zone. Diffusion and convection are the two important mechanism by which the growth is being driven. The key factors for a controlled growth are temperature range and the molar ratio of the precursors which needs to be transported [68]. A transport agent also plays a vital role in the growth mechanism. Generally, Halogen group elements or its compounds are used as transporting agents after sublimation of precursors.

By employing this method, a bulk crystal growth of 2D materials can be done very easily. But creating a Janus structure with a perfect ratio where all the atomic layers are unique is near to impossible, because the parameters that are being used doesn't allow us to control the positioning of individual atom sites as it is more thermodynamically driven, and so there are high chances of creating a randomized structure of two different phases. So, rather than choosing a direct CVT path for Janus growth, the CVT grown bulk 2D crystals (TMDC) can be further exfoliated into monolayers depending on the strength of out-of-plane Van der Waal's interaction compared with the in-plane bonding and then the top atomic layer can be replaced selectively with some post processing methods. Exfoliation can be done either with the help of a mechanical exfoliation technique by scotch tape (as for graphene mentioned above) or liquid phase exfoliation by sonication of bulk crystals.

In case of liquid phase exfoliation, it is difficult to get large lateral size monolayers and, sometimes it is not very easy to remove the solvent completely from the sample after sonication based on the solvent used for sonicating and breaking down the crystal into smaller dimensions. At the same time, the major downside of mechanical exfoliation technique is the limitation of lateral size of the monolayer coverage produced.

Indeed, there is a need of large area monolayer growth which brings our attention to other techniques such as Atomic Layer Deposition (ALD), Chemical Vapor Deposition (CVD) and Physical Vapor Deposition (PVD). CVD will be discussed in greater details showing the effectiveness for growing large scale monolayers on a wafer (substrate).

2.2 Bottom up approach

Since top down approach is not suitable for providing us with a larger lateral dimension of monolayers, researchers were bound to scale up 2D materials at wafer scale.

2D materials synthesis on a large scale has been successfully established using each of the techniques mentioned above.

2.2.1 Chemical Vapor Deposition (CVD)

In addition, with a temperature control for growth in CVT, a CVD system is also equipped with a control over the pressure and gas flow rates during the growth process and so this methodology is more driven with kinetics rather than only thermodynamics.

CVD can be used to perform deposition or coating of any chosen material for enhancing its properties. Precursors are flown over a desired substrate inside the chamber in a gaseous form by subliming them by providing enough thermal energy or directly flowing a precursor gas into the chamber. Chemical reaction occurs on the hot substrate's surface which results in a deposition of thin film over the substrate [69]. This process is accompanied with byproducts which must be evacuated out of the chamber by using a pump and further passing it through a proper reduction system which helps in detoxicating (normalizing) the gases which are being liberated as byproducts.

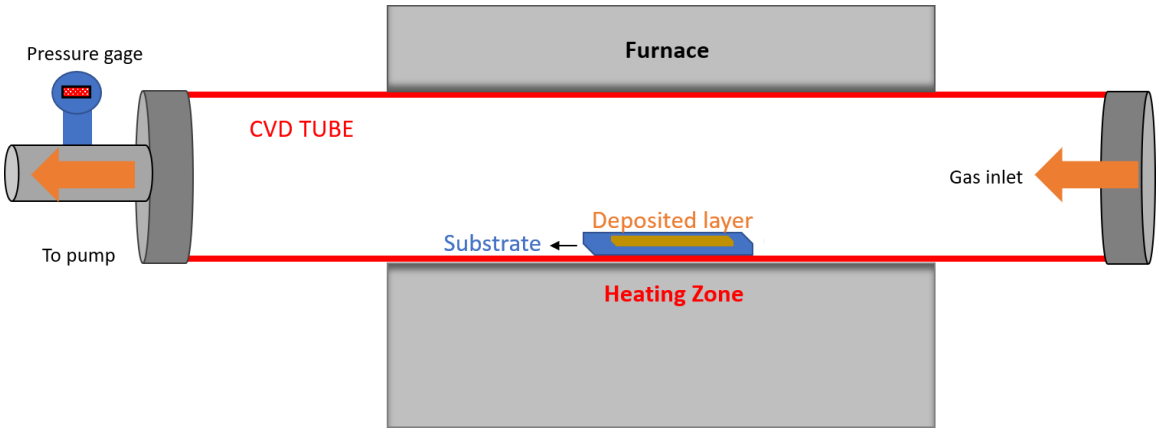

Figure 2.1 Basic schematic for CVD growth

A typical CVD schematic is displayed in figure 2.1. As mentioned before, CVD can be performed at varying pressure levels, ranging from millitorr to atmospheric pressure

which can be controlled by a pump connected to the downstream side of the chamber. There are many different alternatives of CVD available depending on the material that has to be grown, such as atmospheric CVD, MOCVD (Metal Organic CVD), Organometallic Vapor Phase Epitaxy, PECVD (Plasma Enhanced CVD) and many more. In the following sections, CVD has been performed at atmospheric as well as low pressures depending on the requirements.

Sample preparation is also one of the important aspects in growing these films with a better quality. Effective sample preparation can make the substrate more favorable for nucleation which eventually grows into a larger lateral size film over the substrate. Sapphire or SiO2/Si substrates are generally favored because of their high surface energy. Substrates must be cleaned by sonicating them into ethanol for 10 min and then into IPA for another 10 min. After that the substrate are dried off with the help of pressurized blow of nitrogen gas followed by a 5 min of plasma cleaning at the end.

2.3 Plasma processing

Plasma is considered as the 4^{th} state of matter. While gas is electrically insulating, plasma is extremely conductive in nature. Plasma is ignited by ionizing the gas molecules which thus contains ions, electrons and free radicals in it. Every gas has different ionization energies based on the energy required for removing an electron from an atom. In the list of elements, Helium has the highest ionization energy while Cesium has the lowest of all. Plasma is not limited by its property of conducting electricity due to free electrons and ions, but the energy of plasma has also been utilized for several purpose like spacecraft propulsion, sputtering, nuclear-fusion operation, nano-structure fabrication and plasma torches for gas reforming and hazardous gas materials [75].

There are several methods for generation of plasma but here there will be a brief discussion of two kinds of plasma generations methods: Capacitively Coupled Plasma and Inductively Coupled Plasma.

2.3.1 Capacitively Coupled Plasma (CCP)

As the name suggests, that plasma is generated due to coupling of capacitors. Two parallel plates are separated by a distance where it has carrier gas as dielectric medium and a voltage drop is created by an RF or DC source, across the plates which causes the generation of electrical field between the plates in the direction of anode to cathode. Because of this electrical field between plates, electrons are accelerated in the opposite direction with a kinetic energy. These accelerated electrons eventually collide with gas molecules and dissociate them into free radicals (individual atoms). If the energy generated from electrons is high enough then it will also start ionizing the atoms by knocking out electrons from those atoms (radicals) creating a plasma with a color specific to the carrier gas used.

When atoms get ionized, they carry a positive charge and thus they are also accelerated inside the field but in opposite direction of electron. Thus, these ions get accelerated towards the plate which is being grounded. Because of this property, these energetic ions can be used for etching/removing a material which is kept on the grounded plate by bombardment. The rate of etching can be manipulated by controlling the density and energy of plasma. The density and energy of plasma depends on several parameters such as pressure inside the chamber, amount of carrier gas available to ionize, choice of gas, applied RF or DC voltage across the plate and few others.

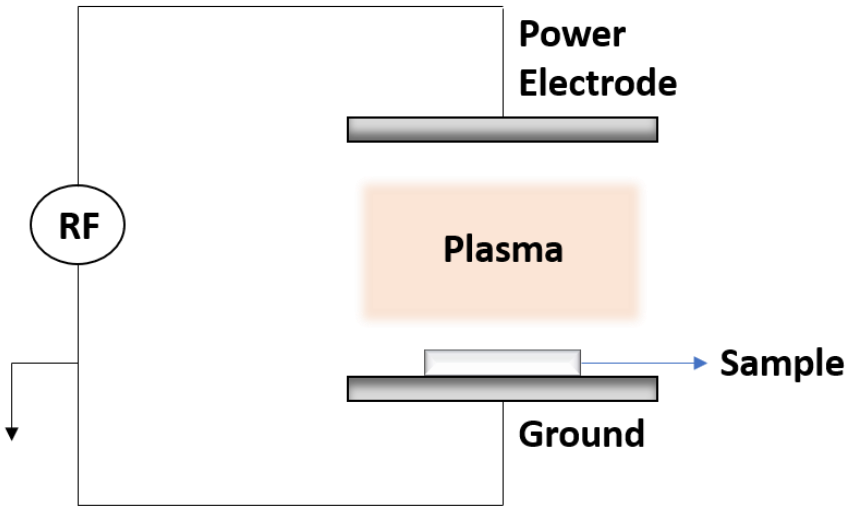

Figure 2.2 Basic schematic for CCP plasma generation

Due to the acceleration of ions in the direction of the sample (grounded plate), even after controlling all the parameters mentioned above in an optimal fashion, it could be very difficult to control the etching rate for a structure containing only three atomic layers having a height less than 1 nm. Therefore, this may cause over etching for such a requirement of gentle rate of removal for single atomic layer.

2.3.2 Inductively Coupled Plasma (ICP)

In ICP, the plasma is sustained by inductive power coupling by following Faraday's law of induction. Thus, it has many advantages over a capacitively coupled plasma, such as low ion damage and a very tailored control on plasma density and ion energies which helps in controlling the etching rate when in sub-nano scales. Due to these reasons, ICP is getting much attention in solar cell/semiconductor/display technology plasma processing for etching or deposition and various other applications such a mass spectroscopy [75].

The principle for ICP setup is the generation of plasma by applying RF power on a helical shaped copper coil (tesla coil) wound around a dielectric chamber (cylindrical quartz tube) having low pressures (in mTorr) with a flow of carrier gas which can be

ionized. Generally, a fixed Radio Frequency (RF) of 13.56 MHz is applied on the coil with a defined power value. Because of which a changing magnetic field is induced by the coil covering a range of distance which eventually creates an electrical field. This magnetic and electrical field now accelerates the electrons inside the cylindrical vacuum chamber. Due to this, these electrons dissociate and ionize the carrier gas molecules depending on the energy provided by that electron as shown in figure 2.3.

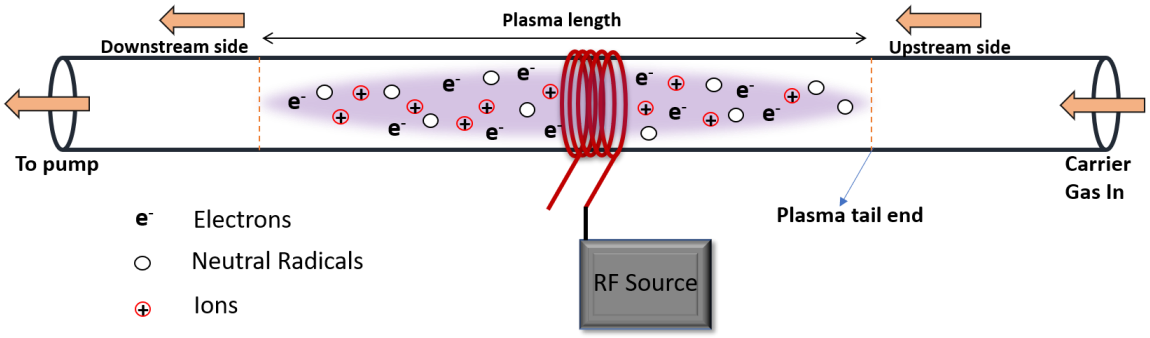

Figure 2.3 Schematic for basic ICP plasma generation

There are several critical parameters that might affect the plasma characteristics and thus affect the overall outcome of the process. Parameters like pressure, gas flow rate, carrier gas that is being used and power from RF source are the most important which must be manipulated according to our needs. Apart from this, number of windings in a tesla coil (helical copper coil), diameter of the coil and diameter of the wire which we use for making a tesla coil, and tube wall thickness (dielectric) that we use also has an accountable effect on plasma density and the energy of plasma [70][71][72].

But here it will be assumed that the parameters of coil and tube wall thickness are constant, to ease the explanation. We may start by keeping the number of winding in a coil as constant and then control the other parameters according to our requirements. But before that we should be aware that the number of windings will dictate the extent and

strength of magnetic field generated while applying RF. It means, if a smaller number of winding were to be used then the intensity of magnetic field will be weak as well as the extent of magnetic field will be smaller. So, the power needed to generate a plasma will increase. Higher power for ignition of plasma means higher energy provided to the plasma which gives more kinetic energy to the ionized gas from the start. On the other hand, if we use large number of windings then we may use low power for generating plasma, but the extended magnetic field range would create a strong plasma even at very low powers and the effect of magnetic field will be seen beyond the length of plasma. This magnetic field can cause ionization and dissociation of gas molecules to a very far extent which cannot be observed by naked eyes. So, we must choose an optimum number of winding which can balance both the effects.

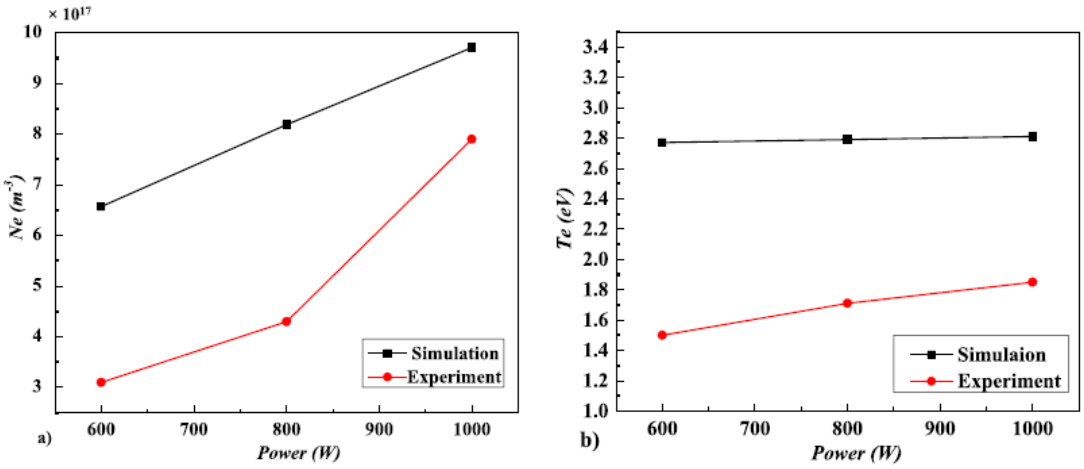

Figure 2.4 Electron density (left) and electron temperature (right) dependence on applied power [70]

Considering coil windings to be constant, we can further think of other parameters mentioned above. As can be seen from figure 2.4, increase in power leads to increase in electron density (left) which causes higher density of plasma. Also, with the increase of

power the temperature of electron increases (right) which leads to increase of temperature for overall system due to scattering and bombardment.

In a similar way, plasma density is also dependent on the pressure inside the chamber. When pressure is increased with all the other parameters to be constant, initially the density of plasma increases due to the increased amount of gas molecules available. But if the pressure is increased further, then the density of plasma starts to decrease because of higher rate of scattering due to too much of atomic interactions taking place. In the same way when gas flow rate is increased while keeping other parameters to be constant, after a certain threshold of increasing density of plasma, the scattering increases which results in low density of plasma. It is also important to note that the selection of carrier gas is the most crucial part of this process because of the atomic size and weight of an atom, as it can decide the rate of etching and energy required for ionization of that element.

All these parameters should be controlled very efficiently to strip a single atomic layer of element such that it doesn't bother the second atomic layer just below it.

2.4 Raman spectroscopy

Raman spectroscopy is one of the nondestructive vibrational spectroscopic technique which has been used to analyze fingerprint peaks of materials. Though it is not only limited to fingerprint peaks, but also it could be used to analyze the defect concentration, crystallinity as well as strain induced in a material at microscopic level.

Since it uses an optical microscope, it can act as a very powerful tool for characterization of thin films and even monolayers (~1 nm thickness). It can be performed on any kind of crystalline structure but, won't be useful if the sample has an amorphous

nature. As indicated in figure 2.5, there is a laser pin hole at the bottom right corner from where an incoming monochromatic laser enters the system from a laser source. It is further directed with the help of mirrors and filters, and further incidents onto the sample through a microscope objective which then scatters back to the same path and Rayleigh scattered or elastically scattered light filters out with the Rayleigh rejection filters and the remaining non-elastically scattered light (from phonon interaction) is detected with the help of a photo detector (spectrometer). This non-elastically scattered light comprises of stokes and anti-stokes scattered rays depending upon the type of interaction of incident light (photon) with phonon within the sample. At room temperature conditions, probability of getting a Stokes shift is much more pronounced than anti-stokes because anti-stokes process requires extra amount of work to be done by phonons.

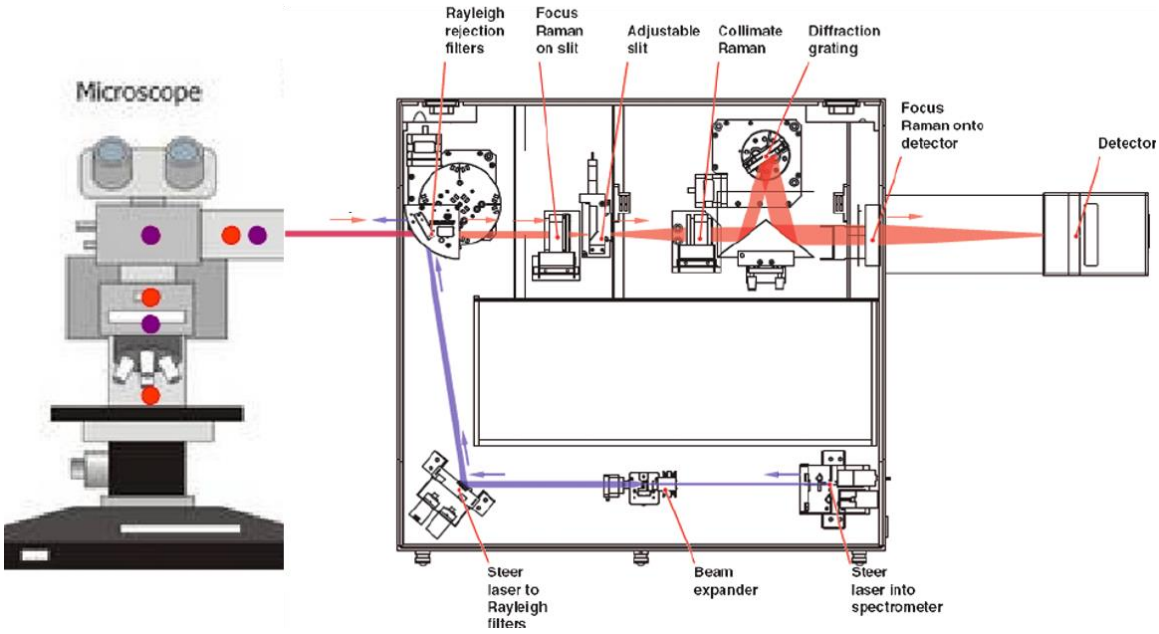

Figure 2.5 Basic schematic for Renishaw Raman spectroscopy © Renishaw

These stokes and anti-stokes (figure 2.6) processes are detected by the spectrometer which causes emergence of peaks on the screen with respect to a certain wave number

(frequency) indicating a particular mode of vibration from the material's symmetry, which can then be compared to either fingerprint signals or from a theoretical phonon dispersion curve. Since majority of the back scattered light is filtered out as a Raleigh scattering while the rest of them consists of Stokes and anti-stokes signal which is a very small percentage of the overall signal. So, it requires very careful measurements to be taken to enhance signal to noise ratio coming from the sample without extended period of exposure with high power laser. Because high power laser could destroy or burn the sample. Also, high power laser could cause surface modification and thus resulting into false data collection.

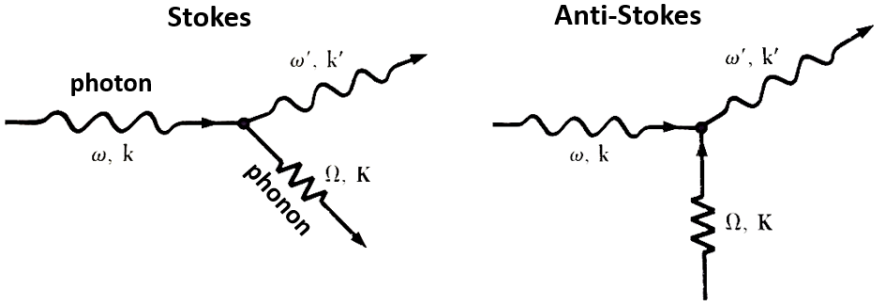

Figure 2.6 Processes indicating Stokes (left) and Anti-stokes (right)

Therefore, measurements should be performed at laser powers as low as possible to avoid any kind of degradation of the sample. Thus, to increase signal to noise ratio, greater number of accumulations can be taken with low laser power.

2.5 Photoluminescence Spectroscopy (PL)

Photoluminescence can also be performed with the same set of instrumentation as for Raman spectroscopy. This technique is mainly dependent on creation of electron hole pairs due to incident radiation of a specified wavelength (or Energy of photon). Here, due to incident photon energy on a material (having a bandgap), the energy of photon is absorbed by electrons and are excited from valence band (VB) to conduction band (CB) if

the minimum energy of photon irradiated on the sample is greater than or equal to the bandgap of that material thus leaving a hole in VB and forming electron-hole pair (when these electrons gets trapped below CB called excitonic level due to phonon). After excitation of an electron from VB to CB, these electrons fall back from CB (excitonic level) to VB in form of a radiative recombination or non-radiative recombination process or a combination of both.

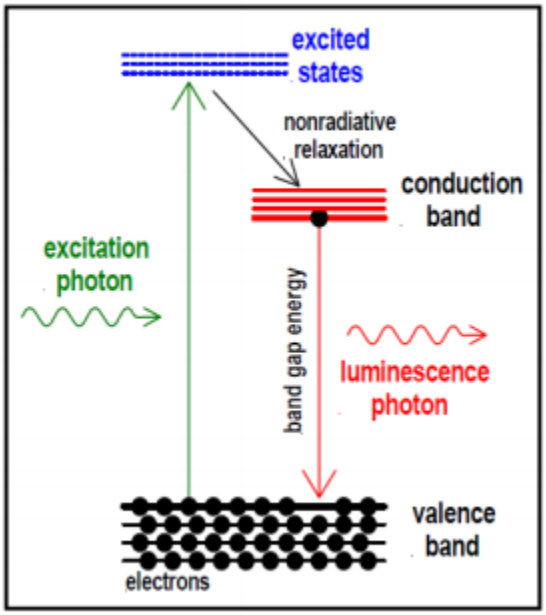

Figure 2.7 Basic principle of photoluminescence spectroscopy

At room temperature conditions for the case of radiative recombination, the energy of the photon emitted is either less than the bandgap or it can be equal to bandgap as shown in figure 2.7. This emitted photon is then collected by the detector and the energy of photon detected can be observed on the screen. Generally, this shows the optical band gap of a material at room temperature conditions. This emitted photon is also helpful in extracting out various other optical properties and defect concentrations.

When low temperature measurements are performed on the sample, the photoluminescence peak energy blue shifts according to Varshni's law [81]. This law states that, there is change in the relative position of the valence and conduction band due to temperature dependent dilation of the lattice, which affects the electron lattice interaction thus decreasing the bandgap of a material at low temperature according to the empirical expression given by Varshni (eq. 2.1), which eventually results in the blue shift of photoluminescence peak energy while going to lower temperatures.

$$E_g = E_0 - \alpha T^2/(T + \beta) \quad (2.1)$$

where α and β are material constants, E_o is bandgap at 0 K, E_g is bandgap at temperature T K.

Apart from this, there is also another type of recombination process known as non-radiative recombination which is assisted by phonons and thus, they produce heat into the material rather than giving photoluminescence. This non-radiative type of recombination is more prominent in case of indirect bandgap materials because excitation and recombination of electron from VB to CB and CB to VB requires phonon help to conserve the momentum. So, this process of characterization by photoluminescence is not an effective approach for indirect bandgap materials.

While for the case of direct bandgap materials we can easily extract out the optical bandgap of the material based on the plot of PL intensity vs energy, where energy value for a peak suggests the optical band gap while FWHM of the peak can be helpful in determining the quality or identify a relative concentration of defects into a material.

2.6 Atomic Force Microscopy (AFM)

Atomic force microscopy is one of the most preferred techniques for metrology measurements such as surface roughness or topology due to its ability to quantitatively measure the x, y, and z direction with nanoscale resolution with a higher precision. While other high-resolution microscopic like SEM or TEM characterization methods rely on interactions of electrons with a material (sample) which might also damage the sample if proper care is not taken. In AFM there is a direct mechanical contact between the tip and sample which enable a very precise measurement of sample's surface morphology. Various parameters exist to qualitatively verify the roughness of sample's surface.

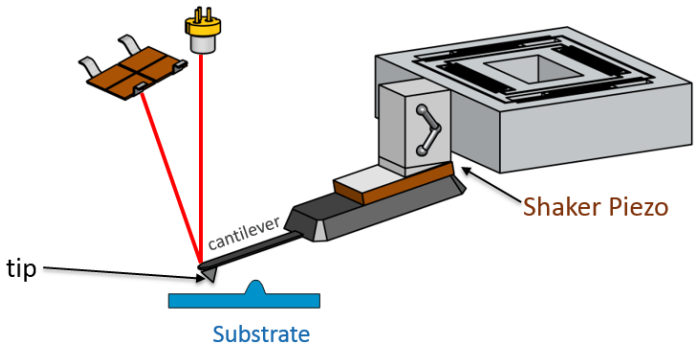

Figure 2.8 Schematic for AFM principle © nanosurf

Principle of AFM is based on the cantilever (tip) assembly that directly interacts with the sample's surface. These cantilever tips are made of silicon or silicon nitride with a conductive or a non-conductive coating at the tip region based on the application of that cantilever. This AFM probe interacts with the sample through a raster scanning motion over the substrate. There is a laser beam reflected from the top of cantilever which monitors the vertical and lateral motions of the AFM tip as it scans through the surface. This reflected laser beam is further tracked by a position sensitive photodetector (PSPD) which picks up the side as well as up/down motion of the cantilever. In order to achieve the AFM modes known as tapping, the probe is mounted into a holder with a shaker piezo

as shown in figure 2.8. Generally tapping mode of operation is performed in resonant modes, where operation is at or near the resonance frequency of the cantilever.

Since AFM is very sensitive to even small dust particles adhering to a sample, cleaning is thus one of the crucial steps before running the measurement. It is always advisable to keep the sample under clean and vacuum sealed environment to avoid any kind of surface dust and dirt because if the sample is very sensitive then it cannot be cleaned which may result into false data sets. After the sample is ready, it has to be transferred on a stainless-steel plate with the help of a silver paste or a double-sided tape which is then mounted on a stage which consist of a magnet on the top to hold the sample during measurement. 512 lines resolution with a slower scan rate must be performed to get a high-resolution image.

Chapter 3 Surface Atomic Layer Functionalization to create Se-Mo-S

3.1 Introduction

As discussed earlier, Janus MoSSe could be grown from previously grown CVD (Chemical Vapor Deposition) samples of MoS2/MoSe2 by post Selenization/Sulfurization processing. There are few parameters that should be considered for the selection on which way to be followed. As we know that there is always a competition between threshold temperature to make a bond for creating a new structure and a threshold energy required for breaking a bond for introduction of defects and decomposition of previous CVD grown sample.

A critical way must be chosen, which will help in replacing only one atomic layer of Sulfur/Selenium from the CVD grown monolayer sample which has Selenium/Sulfur as a topmost layer as we can see from the structural schematic from figure 1.2. Few experiments were carried out which could help in choosing a path from where to start the process of creating a better crystallinity Janus monolayer by an innovative technique described in this work.

3.2 Thermal Sulfurization and Selenization of Sputtered Molybdenum film

Initially, sputtering of Molybdenum film on a c-plane sapphire substrate (1 cm * 1 cm) at room temperature with a magnetron sputtering chamber was performed, creating ~1-2 nm thick layer of Molybdenum on the substrate. Sputtering was carried out in Argon rich environment at 150 mTorr pressure. Oxidation of this molybdenum film is likely to be expected since it was exposed to ambient atmosphere after being sputtered.

The idea behind this was to perform thermal selenization and sulfurization of the sputtered film for determining the parameters that can be used in future for post CVD processing of already grown crystals to accomplish the goal of creating a Janus crystal by replacing the top layer.

Sulfurization of molybdenum film was carried out at different temperatures, ranging from 400 °C to 700 °C, while Selenization was carried out in the temperature range of 500 °C to 800 °C in presence of Sulfur (Sigma-Aldrich, 99.98% purity) and Selenium (Sigma-Aldrich, ≥99.5% purity) respectively at 6 Torr (Sulfur and Selenium were kept in excess quantity). Sputtered substrate was placed on a quartz boat at the center of the furnace and sulfur was placed in a separate quartz boat at 17.5 cm upstream from the center of the furnace, where the temperature of sulfur reached to ~180 °C. In case of Selenization, Selenium was placed in a quartz boat at 16.5 cm upstream from the center of the furnace where the temperature of selenium reached ~270 °C. Sulfurization was done in only Argon environment while Selenization was carried out in presence of Argon gas with a little of hydrogen gas as well. The goal was not only to successfully sulfurize/selenize the molybdenum film but also to select a temperature low as possible such that to avoid provision of excess thermal energy to molybdenum that it starts mobilizing over the substrate. In the series of experiment conducted, it was observed that there is a threshold temperature at which the mobility of molybdenum atom over the substrate can be avoided but could still sulfurize/selenize the sample successfully. The aim was not to form good triangular flakes or continuous film growth but to get weak signals from MoS_2/$MoSe_2$ vibrations after Sulfurization/Selenization.

Longer time of growth was avoided because this procedure was expected to be adopted in future for post CVD processing of CVD grown monolayer samples. If much

longer time were to be used, then the chances of creating S/Se vacancies could increase very rapidly and thereby replacing most of the chalcogenide atom sites with Se/S depending on the path chosen.

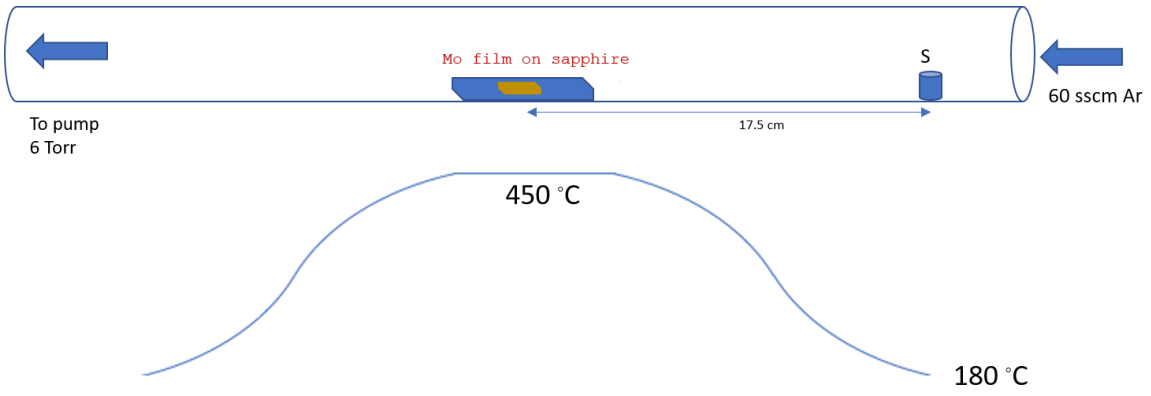

Figure 3.1 Schematic for thermal sulfurization of Mo film and it's temperature profile

In case of Selenization, the minimum temperature required to selenize the film was 580 °C, when Selenization was performed for 30 min at 6 Torr with a gas flow rate of 60 sccm (55 sccm Ar and 5 sccm H2). Since presence of Hydrogen gas is needed while selenization process, there are always high chances that the chalcogens are being etched simultaneously during growth period. Hydrogen is helpful in reducing the oxides of Molybdenum but at the same time the effect of excess etching of Selenium during this process should also be considered, since it can easily form H_2Se gas if the amount of hydrogen is not controlled accurately [79].

It was observed that sulfurization of molybdenum film was easier even without giving enough energy for molybdenum to become mobile over the substrate. Figure 3.2 indicates optical images of formation of MoS2 on sapphire substrate from a sputtered molybdenum film, where fig (a) shows sulfurization done at 630 °C while fig (c) shows the sulfurization done at 500 °C at 6 Torr for 30 min with the Argon gas flow rate of 60 sccm.

The temperature was lowered even further to 450 °C where the Raman peaks from MoS2 were still showing up without even seeing a nucleation site or a flake formation unlike we see in fig (a) and (c).

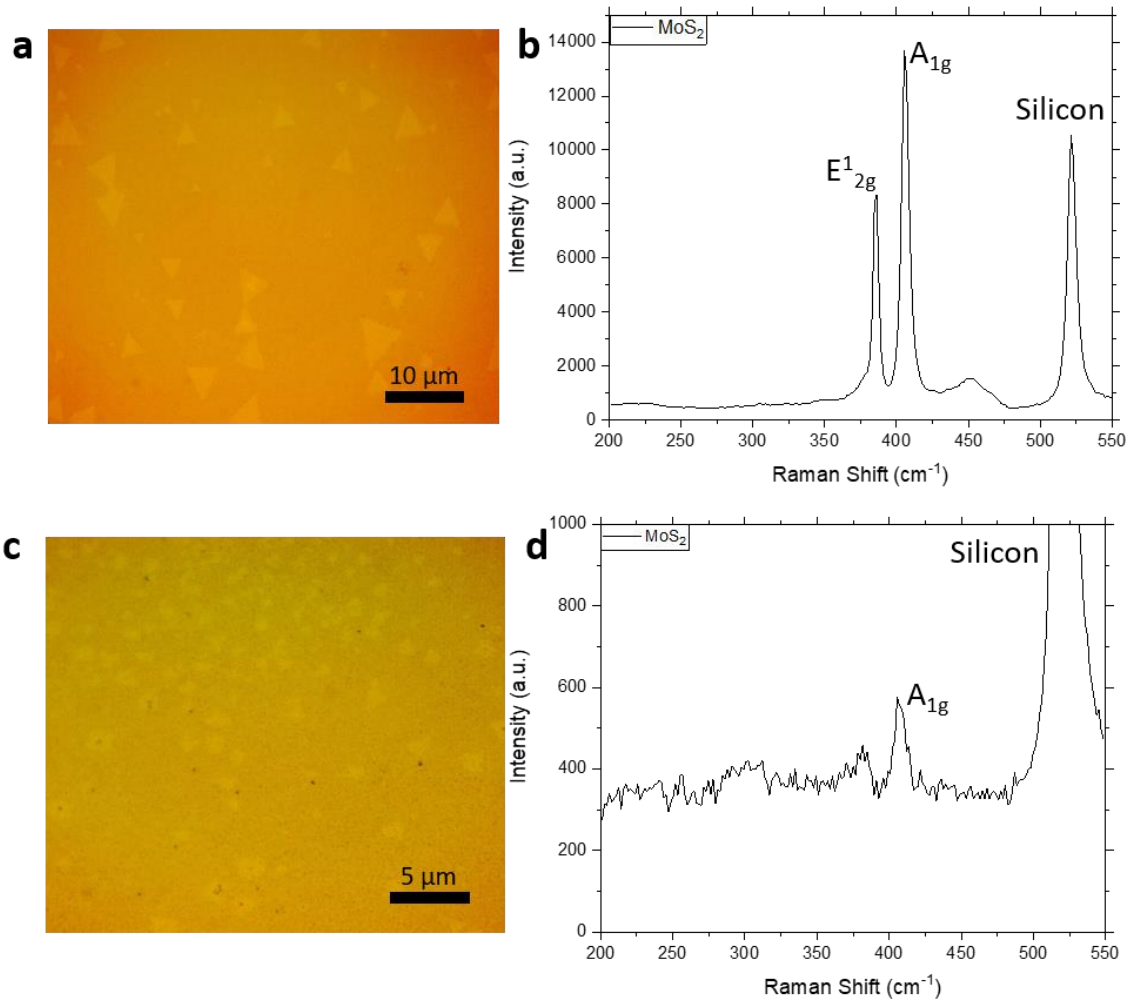

Figure 3.2 (a), (b) Optical image of thermal sulfurization for Mo film at 630 °C and the corresponding Raman signal (c), (d) Optical image of thermal sulfurization of Mo film at 500 °C and it's Raman signal

From the above experiment, it can thus be concluded that CVD MoSe2 monolayers must be grown at first, followed by a post CVD procedure of thermal Sulfurization for replacing the top layer of selenium with sulfur and at the same time avoiding bottom atomic layer vacancy creation due to thermal energy.

3.3 Growth and characterization of MoSe2

Synthesize of single crystalline monolayer MoSe2 was done on a 90 nm SiO2/Si substrate by using chemical vapor deposition method. MoO3 powder (Sigma-Aldrich, ≥99.5% purity) and Se powder (Sigma-Aldrich, ≥99.5% purity) were used as the precursors for carrying out CVD reaction. A 90 nm SiO2/Si substrate with an area 15 mm × 5 mm was first sonicated for 5 min in Ethanol and then with Iso-propyl alcohol. After sonication, the substrate was dried by blowing pressurized nitrogen gas flow, followed by 5 min plasma cleaning (Plasma of Argon + Oxygen) inside a plasma chamber. Substrate was then placed in a ceramic boat (polished side facing downward) at the center of the furnace and MoO3 powder (2 mg) containing NaCl (in the ratio of 50:1) was placed in the same ceramic boat below the substrate. Selenium powder was placed upstream in a ceramic crucible (excess quantity) 16.5 cm away from the center of the furnace. The carrier gas was high purity Ar (≥99.99%) and high purity H2 gas with 46 sccm and 4 sccm flow rates respectively.

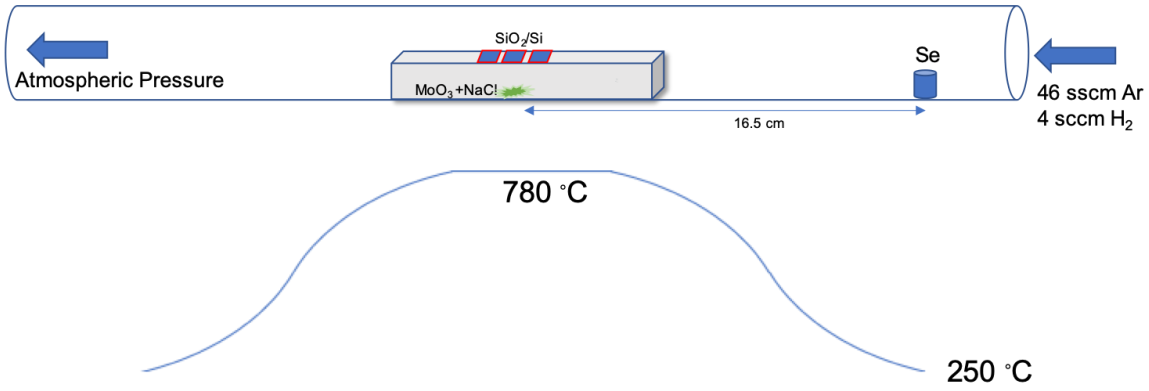

Figure 3.3 Schematic for CVD MoSe2 growth and it's temperature profile

The center of the furnace was gradually heated from room temperature to 300 °C at the heating rate of 50 °C/min and maintained for 10 min. After a 10 min substrate impurity cleaning stage at 300 °C, the temperature was raised to 780 °C at the heating rate

of 60 °C/min. The temperature of Se powder was simultaneously raised to ~260 °C. After the growth period of 14 min at 780 °C, the hydrogen gas flow was stopped to avoid over etching of selenium from the grown flakes and then furnace was allowed to cool down naturally to room temperature at the rate of 10 °C/min. The sample was taken out of the growth tube after furnace reached room temperature and then was observed with a microscope and various other characterization techniques.

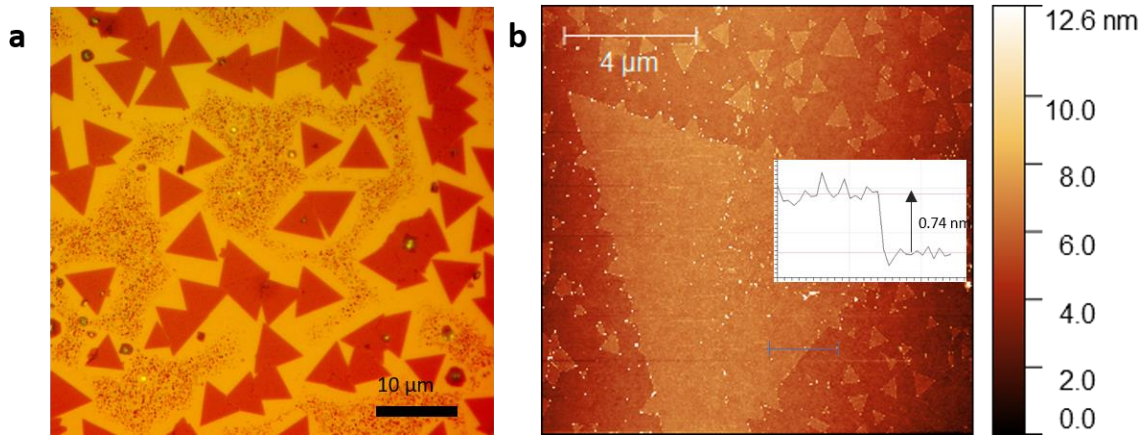

Figure 3.4 (a) Optical image of CVD grown MoSe2 (b) Topology and height profile of CVD grown MoSe2 by AFM

3.3.1 Atomic Force Microscopy

Since it is very important to know whether the growth is monolayer, as the future goal was to make a Janus structure where it is utmost necessary not to have more than single layer because of the reason that the process that has been adopted is only applicable for successfully replacement of only top chalcogenide layer. Topology and height profile were measured by AFM to check if they were monolayers. NT-MDT AFM setup was used in a non-contact tapping mode with a non-conductive AFM tip (cantilever) and scanning was performed in normal ambient conditions. A raster scanning of CVD grown MoSe2 samples on SiO2/Si was done with a resolution of 512 x 512 considering 512 points per line.

As shown in the figure 3.4 (b), the thickness of these flakes was observed to be ~0.74nm, which confirms it to be a monolayer structure.

3.3.2 Raman Spectroscopy

Quality of MoSe2 was examined by Raman and PL spectroscopy measurements as shown in the figure 3.5. All the measurements were carried out with Renishaw inVia Raman setup with a blue laser source of 488 nm wavelength. The data was taken for 5 sec of exposure time on sample (MoSe2 flake) with incident laser power controlled at 5% and 5 accumulations were taken for increasing signal to noise ratio. As per from the Raman signal observed, two major peaks could be observed which are indicated at ~242 cm^{-1} and ~286 cm^{-1} in the plot. Peak at 242 cm^{-1} is an out-of-plane vibration mode known as A^1_g mode while a peak at 286 cm^{-1} is an in-plane vibration mode which is known as E^1_{2g} mode of vibration. These peak matches the previous literatures characterization. There are also other modes that could be observed based on the incident laser wavelength that is chosen [78]. Additional Raman peak at 520 cm^{-1} is from silicon substrate.

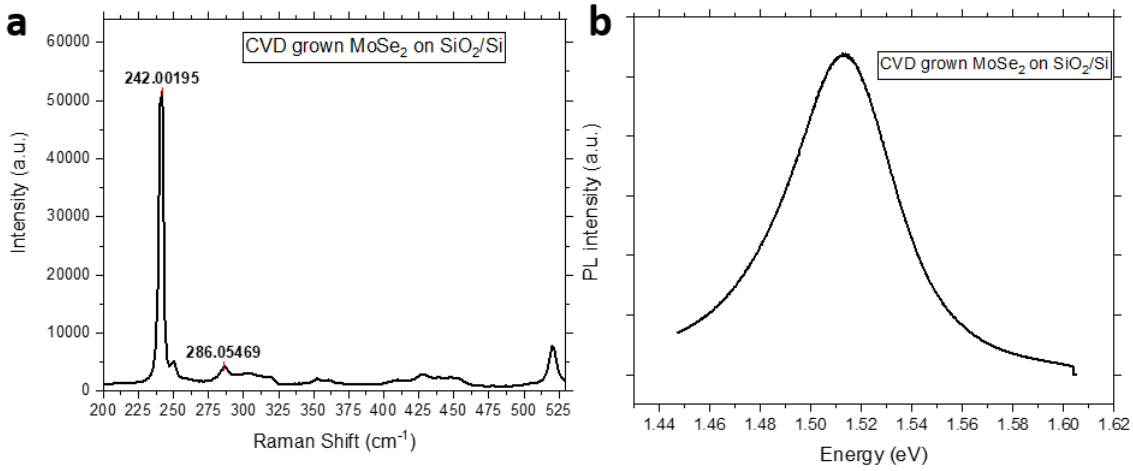

Figure 3.5 (a) Raman peaks for CVD grown MoSe2 (b) PL peak for CVD grown MoSe2

3.3.3 Photo Luminescence (PL) Spectroscopy

Measurements were carried out with the same setup as for the Raman described above. PL intensity was collected for monolayer MoSe2 CVD grown samples for 5 sec of exposure time with 5% laser power and taken 5 accumulations for increasing the signal to noise ratio. The PL peak position was found to be at ~1.515 eV which is close to the claim of other previous literatures [77]. There is a little red shift of peak position observed in these CVD grown samples as this process has comparatively a faster rate of cooling which induces strain in the flake due to difference in thermal expansion coefficient of substrate and the flake. This strain effect could be proved by acetone decoupling method [76] which helps in decoupling the monolayer flake from its's substrate by dropping a single droplet of Acetone/IPA on the substrate. This could be observed from the following comparison done for the same sample (same flake); before and after dropping an Acetone/IPA droplet.

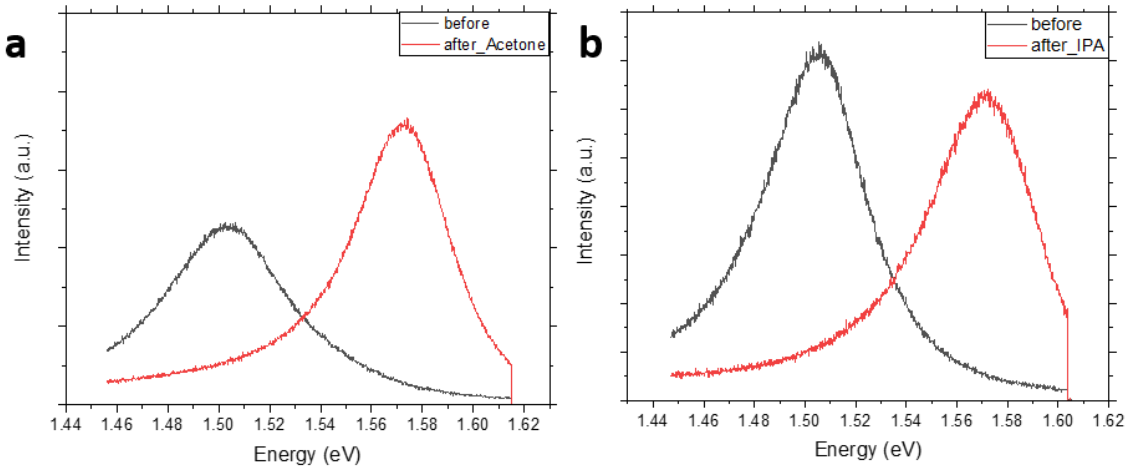

Figure 3.6 (a), (b) PL peak shifts for before (black) and after (red) MoSe2 Acetone and IPA decoupling

PL was measured with 1% laser power for 5 accumulations with 5 sec of exposure time before Acetone/IPA treatment and then an Acetone/IPA droplet was dropped with a micro pipette onto the substrate which dries within 10 minutes. The same flakes were measured after 15 mins with same parameters and the PL peak position blue shifted from 1.51 eV to 1.57 eV which is a very significant shift of ~60 meV. And this experiment was repeatable when done for MoSe2 flakes with 1.51 eV as the PL peak position on SiO2/Si substrate, which concludes that this is due to a strong substrate and sample interaction causing strain inside the samples.

3.4 Direct Sulfurization of MoSe2

Sulfurization was carried out for the previously grown CVD samples of MoSe2 at ambient pressure with an Argon gas flow rate of 60 sccm in the temperature range of 450 ˚C to 850 ˚C for 10 to 30 min of growth time in respective experiments. Substrate was kept at the center of the furnace while sulfur was kept upstream at 18 cm from the center of the furnace where the temperature ranged between 180 ˚C to 210 ˚C based on the furnace temperature used during actual growth.

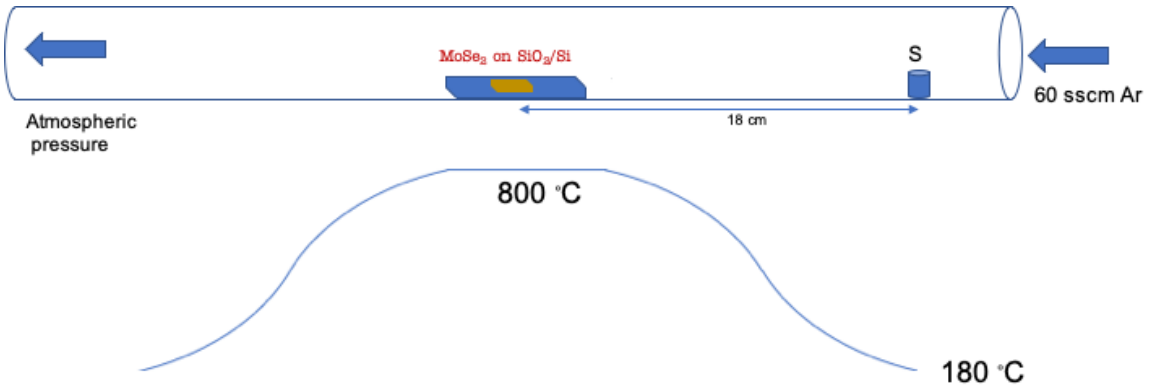

Figure 3.7 Schematic for direct thermal sulfurization of CVD grown MoSe2 and its temperature profile

Based on the previous literature for Janus MoSSe [66], similar parameters were applied for Sulfurization between 750 - 850 ˚C at ambient pressure conditions for 20 min and MoSe2 flakes completely turned into MoS2. Rather than forming a Janus structure it gave enough energy for breaking the bonds between Molybdenum and Selenium while making molybdenum mobile enough on the substrate which resulted into emergence of new flakes which were totally converted into MoS2. If the temperature of sulfurization was below 700 ˚C for 20 min, it was observed that the flakes were still showing Raman peaks of MoSe2, but the intensity was lower in comparison to the intensity measured before, due to expected defect generation from thermal energy.

There were few critical temperatures between 700 - 800 ˚C where, weak Raman peaks from Janus structure as well as strong peaks from MoSe2 and MoS2 were observed when sulfurization was performed for 15 min, which indicates the time of sulfurization has also a very significant effect. So, the structure was partially converted to JANUS with a random formation of MoS2 while containing the remnants of MoSe2 from the original structure. This indicated the increase of Selenium vacancy with higher temperature introduced random formation of Janus (SeMoS) as well as MoS2 structures. And the

results for sulfurization below 700 °C showed weakening of MoSe2 intensities (due to defects) and introduction of very weak MoS2 Raman peaks with no other significant Janus signals. So, because of the high temperature approach, this process is not a very controlled way for replacement of single atomic layer.

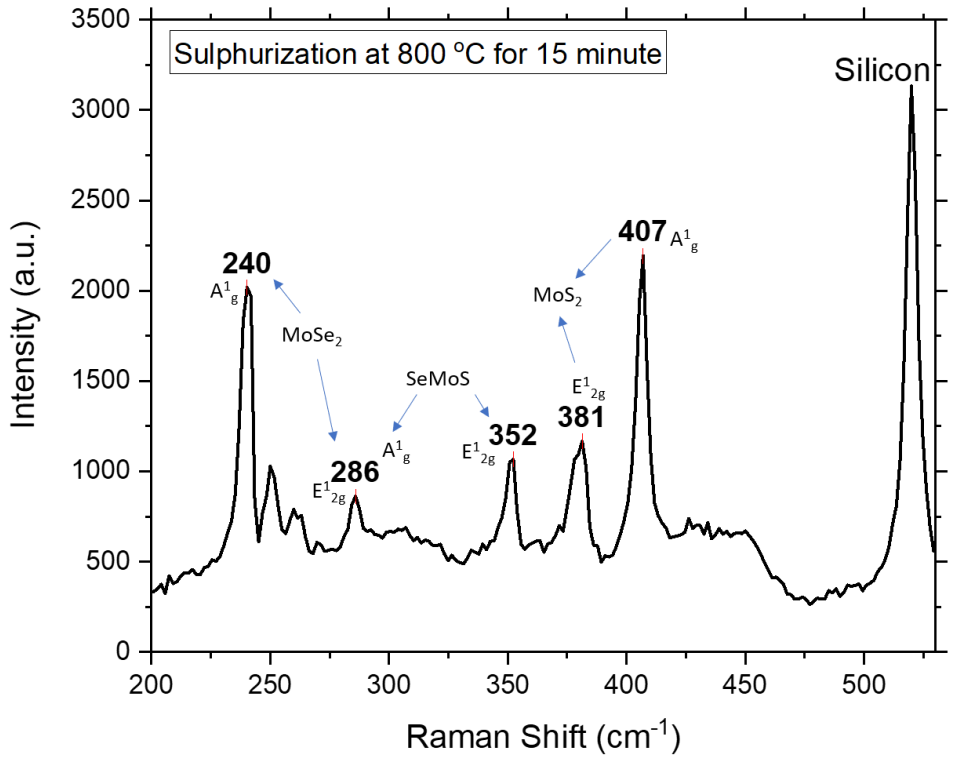

Figure 3.8 Raman signals after direct thermal sulfurization of CVD grown MoSe2

To avoid this kind of randomized formation of all the phases together (MoS2/MoSe2/SeMoS), the top layer Se should be etched and thus, S layer can easily be replaced on top of MoSe structure at even low temperatures. So, plasma stripping method for stripping off the top layer of Selenium from MoSe2 and then performing thermal sulfurization was considered for further experimentation.

3.5 Plasma etching

The most critical thing we must choose for plasma etching is the carrier gas that should be used to create plasma. It is very important to note that we should be able to choose a gas such that it can be ionized with low power and the element shouldn't have too much of atomic mass. Also, we always have to take care about the reactivity of the species of plasma with the sample which is getting stripped. This approach is based on reactive ion etching principles which helps us to achieve selectivity of etching a specific element much easier and faster than other elements from the structure, by making the initial bonding of that selected element weaker with the parent structure and form new bonds with the plasma species (radicals) by surface adsorption phenomenon.

$$2H + Se \rightarrow H_2Se(g) \tag{3.1}$$

Considering the above criteria, Hydrogen was adopted as a carrier gas which is the lightest element of all. When we generate plasma, it creates H^+ ions and excess of H radicals. For the case of MoSe2, these H radicals gets adsorbed on the top atomic layer of chalcogenide (Selenium) which results in weakening of bond of Mo (below chalcogenide) with the Se top layer. Further, these chalcogens which adsorbed the H radicals gets easily knocked off by energetic bombardment of H^+ ions (from plasma) which are being accelerated due to the electrical field inside the plasma. The kinetic energy of the impact (mostly ions) is transferred into internal energy and is redistributed among the bonds as rotational and vibrational form of energies.

$$e^- + H_2(g) \rightarrow 2H(radicals) + e^- \tag{3.2}$$

$$e^- + H \rightarrow H^+ + 2e^- \tag{3.3}$$

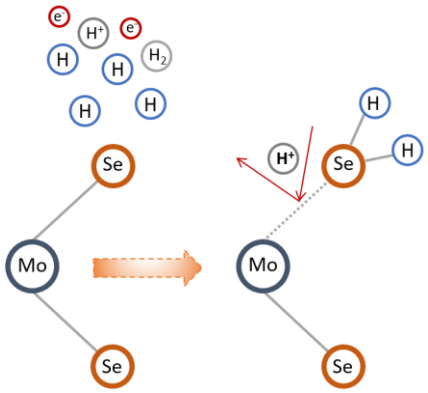

Figure 3.9 Schematic showing Reactive Ion Etching (RIE) by plasma for CVD grown MoSe2 monolayer

As indicated in figure 3.9, during this process, if this internal energy is higher than the bonding energy of chalcogenide with the transition metal then the ion fragments along this bond which eventually results in chalcogenide vacancy at that site. In this process we have to use RF power as low as possible since the density and energy of plasma increases with power which eventually results into a very random and harsh impact of ions on the sample. High energy and dense plasma may result in severely cracking and destroying a nanometer thick sample. Based on this, there were number of experiments carried out which are being discussed in the later sections.

3.5.1 Inappropriate/Over stripping by plasma

We have already discussed about the principles of etching and the parameters which we should be concerned while etching a layer so gently that it only etches one single atomic layer from top, out of a 3 atomic layer structure of MoSe2. Here the focus would be to make a good Janus (polar) structure while trying to strip the top selenium layer from CVD grown MoSe2 monolayers by hydrogen plasma and further replacing it with sulfur by thermal sulfurization in a controlled environment.

Firstly, stripping was performed with the help of plasma cleaner setup, the sample were kept directly inside the plasma chamber where plasma is being generated (in case of direct plasma mode) or it could be placed downstream to the plasma generation chamber by using a remote plasma mode. While using these modes in plasma cleaner, the sample (CVD grown MoSe2 monolayers) was being over-etched even when it was kept for a duration of 1 min because of huge number of ions getting impacted over the sample in a very short duration of time. The SEM image in figure 3.10 (a) shows the energetic impact of ions on MoSe2 monolayer sample when kept in a remote hydrogen plasma chamber for 1 min causing severe cracks on the whole flake.

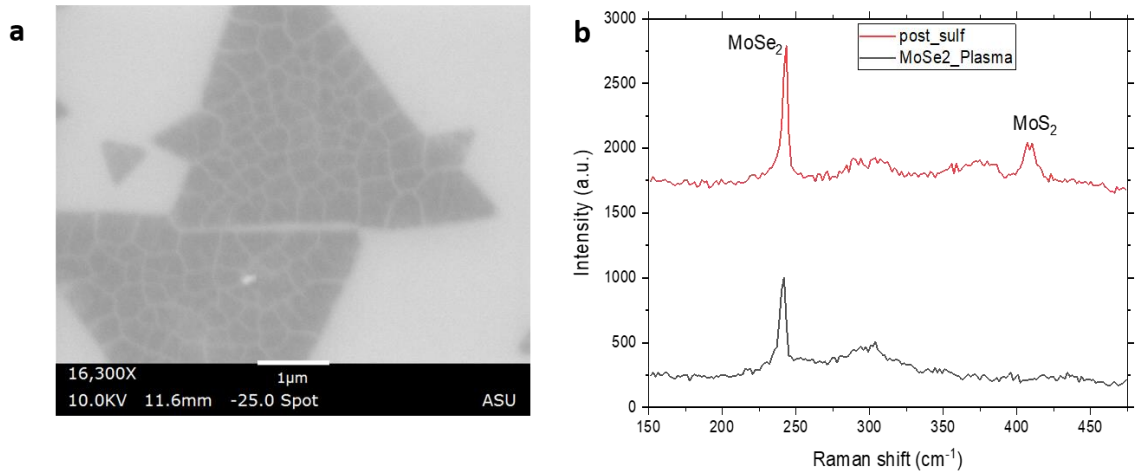

Figure 3.10 (a) SEM image for over-etched MoSe2 monolayers displaying severe crack formation (b) Raman signals from plasma etched MoSe2 (black) and after it's post thermal sulfurization (red)

After plasma stripping process, the flakes were being characterized by Raman/pl and there were small Raman signal (peaks) of MoSe2 still seen, which means the sample was definitely being etched in the process as the intensity of Raman peak fell from 65000 units to ~700 units. If ex-situ thermal sulfurization was being carried out for these samples in a huge temperature range, from 450 °C to 800 °C, the results for sulfurization temperatures below 550 °C for 30 min showed emergence of small MoS2 Raman peaks

with presence of previous $MoSe_2$ peaks as well, but no signals were observed from a Janus structure. At higher temperatures it completely turned into MoS_2 flakes.

The plasma generated in this plasma cleaner setup is from a capacitively coupled plates (CCP plasma), where the sample are kept on a grounded plate which causes acceleration of positive ions toward the plate and thus increases the kinetic energy of those ions. This creates very powerful etching and so it was not very convenient way for etching only one atomic layer from the top.

Apart from this, when the sample is taken out from the plasma chamber, the etched sites of molly have a higher chance to have oxide states on the surface due to ambient exposure. The cohesive energies for bonding between Mo with oxygen must be much higher than that of Mo with Se or S due to which ex-situ sulfurization is not a very plausible path to succeed. Since the cohesive energies are in the following order, Mo-O > Mo-S > Mo-Se [73], [74]; it is most likely that the sample starts stripping selenium sites while trying to replace the oxygen sites with sulfur on the top layer during post thermal sulfurization process. So, if the temperature is less, then the bond of Mo with oxygen can't be broken and when thermal energy is increased enough to break the bonds of oxidized states with Mo, then the sample starts losing Se with a high rate. So eventually either the sample always forms mixed structure of $MoSe_2$ and MoS_2 at low temperatures or it completely turns the sample into a new MoS_2 flake by giving enough energy due to high temperature. Since the cohesive energies for Mo-O bond is higher than that of the Mo-S or Mo-Se sites [73], [74], it is presumably difficult to strip only oxygen sites and keep the rest of the structure intact.

To avoid these difficulties, a gentle stripping method was developed with an in-situ sulfurization methodology.

3.5.2 ICP stripping with Plasma Enhanced Replacement

New form of plasma generation was adopted with an inductively coupled plasma (ICP) setup for making the stripping process gentler. A long quartz tube with 1" inner diameter was used for the purpose of ICP plasma stripping with an additional setup to also perform in-situ sulfurization after stripping.

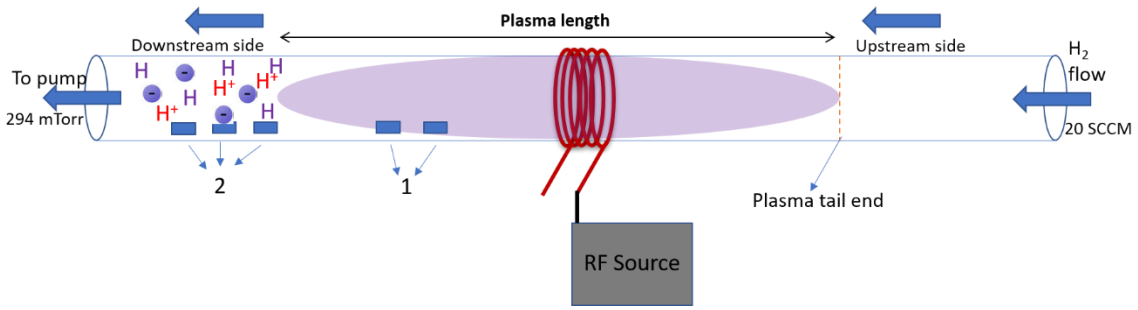

Figure 3.11 Basic schematic for ICP plasma stripping process

Stripping was carried out by flowing H2 (99.99%) as a carrier gas at a flow rate of 20 sccm for plasma generation. The pressure was maintained at 294 mTorr and RF power of 15 W was applied to a helical shaped copper coil (with five turns), wound on the quartz tube.

Stripping of Se from the top of CVD grown monolayer MoSe2 was performed with this setup while keeping the samples towards downstream region (which is indicated by 2 in the figure 3.11) and was also kept inside the plasma (indicated by 1). The etching was performed in the range of 1-5 mins while keeping rest of the parameters as constant. Further, these samples were characterized with help of Raman to observe the intensity reduction from the stripping process as done before. This process should be followed to find an appropriate region and time to keep the sample substrate while performing in-situ sulfurization. The samples should be kept in the same place where the lowest intensity of MoSe2 Raman peaks was observed. While performing in-situ sulfurization for these

samples it was observed that the results were similar to what was observed while performing stripping through a plasma cleaner with post ex-situ sulfurization. This shows that the samples could either get under-etched when kept for a short duration of time or they could get over etched when they are kept inside the plasma or downstream of the plasma. This could arise due to excess of ions flowing over the downstream region from the plasma (as well inside plasma), which might destroy the sample completely or it could etch the sample in a very random manner. Here, random etching implies etching of both top and bottom layer of Se simultaneously at some regions on a flake which causes diffusion of Se atoms around the flake. All the situations mentioned above does not have any effect of sulfur during the plasma etching process.

As discussed, that there was over etching of monolayer $MoSe_2$ flakes when kept at downstream region in case of ICP plasma setup, and sulfur effects were avoided into the system by keeping it further away on the upstream region while plasma etching, the following section will be more focused on how to avoid over etching and how the presence of sulfur helps the creation of a Janus structure during the etching process, indeed turning the simple plasma etching process into plasma enhanced replacement process.

Stripping must be as gentle as possible to avoid over-etching as well as randomized etching. Also, if the top layer of Se is getting etched, there will arise a high concentration gradient of Se atoms in the vicinity of ~0.5 nm, which drives the diffusion of some of the bottom selenium atoms to the top of Mo. As the etching continues, the ions also starts knocking the bottom Se atoms. Since the Mo sites become very active during stripping of Se from top, it eventually leads into strong diffusion of Se and re-emergence of $MoSe_2$ in some regions of that monolayer in a randomized manner. In this way, it is never possible for this process to completely strip of the top layer of selenium and wait for S to bond in

the next step of in-situ thermal sulfurization because diffusion will start simultaneously with the etching process. This may also result in a non-uniform Janus formation which always has some remnant of parent structure (as MoSe2/MoS2 in case of Janus SeMoS).

To avoid this kind of diffusion during the etching process, an innovative technique of plasma enhanced replacement (PER) was developed which replaces the top Se atom with sulfur instantaneously during the process of etching.

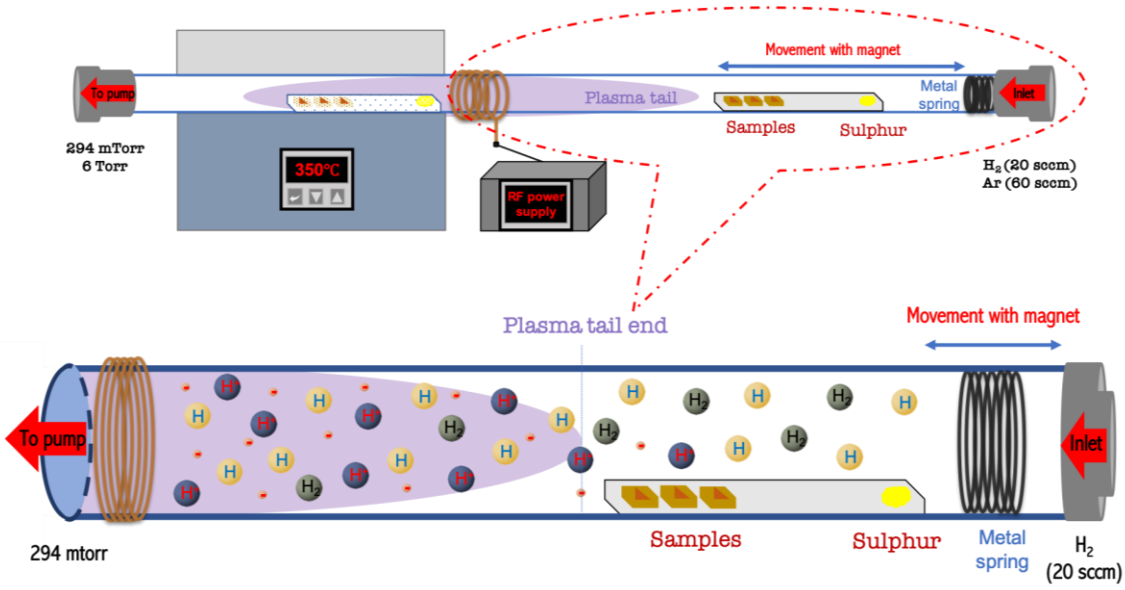

Figure 3.12 Detailed schematic showing setup for PER sulfurization with in-situ sulfurization (top) and upstream plasma enhanced replacement sulfurization (PERS) methodology

Since the method of ICP plasma follows the principle of generation of plasma based on the induced changing magnetic and electrical field generated by an RF source, the strength of this induced magnetic and electrical field which accelerates electrons inside the chamber decreases with distance. Thus, the carrier gas is able to ionize as well as dissociate beyond the length of plasma on downstream as well as upstream region as indicated in figure 3.12. This helps in stripping the top layer of selenium at extremely slow pace when sample is kept at upstream region with a certain distance away from the plasma

tail end. So, sample was kept in a quartz boat, 3 cm upstream from the plasma tail end while sulfur was kept 20.5 cm upstream from plasma tail end in the same quartz boat. RF power of 15 W for an ICP setup was applied to generate hydrogen plasma at 294 mTorr pressure for 8 min.

The reason behind using Sulfur during the etching process itself is that, to try to replace as many Se sites as possible with a new stable structure having S at the top. So, it is very important to keep S at an optimum distance upstream from the plasma tail end. This distance is mainly decided based on the RF power of plasma and the number of winding of the helical coil used in the process, as well as all the other parameters that were mentioned which affects the length and density of plasma.

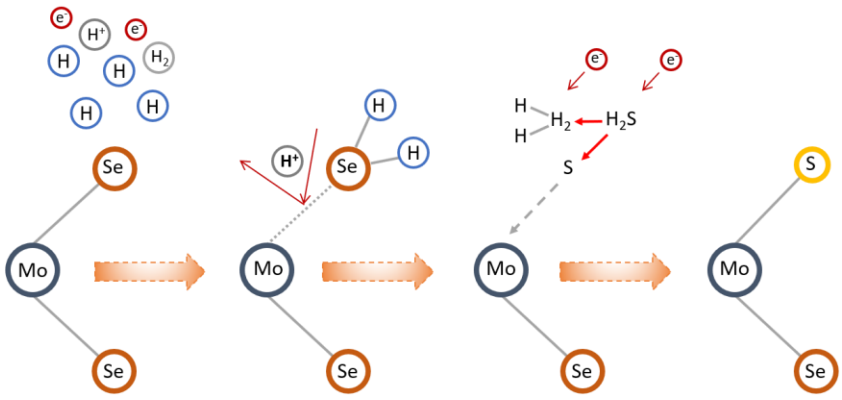

Figure 3.13 Schematic indicating individual reaction roles during plasma enhanced replacement sulfurization process

Dissociation of a molecule into free radical requires significantly less energy than ionization. So, the extent of hydrogen radicals is far beyond the plasma that could be observed visually. These hydrogen radicals are highly reactive in nature and thus they get easily adsorbed on the surface of sulfur. This deliberately helps in formation of H2S gas when passing from the top of sulfur kept at a defined distance upstream from the plasma edge. Apart from that, there is also some hydrogen ion formation beyond length of plasma,

but the quantity of ions is far less than it is in the actual plasma region. This will eventually help in carrying H2S gas molecules over the sample substrate where the magnetic field and electrical field strength increases as it is approaching near the coil. The energy generated from the coil is enough for the dissociation of H2S molecule and creating sulfur radicals. The process of formation and dissociation of H2S continues while passing over the sample substrate.

$$2H + S \rightarrow H_2S(g) \quad (3.4)$$

$$e^- + H_2S(g) \rightarrow H_2 + S\ (radical) + e^- \quad (3.5)$$

Table 1 Ionization and dissociation energies for the species

Species	Ionization energy (eV)	Dissociation energy (eV)
H	13.59	-
S	10.36	-
Se	9.75	-
H_2	-	2.27
H_2S	-	2.7
HS	-	1.95
H_2Se	-	2.36
HSe	-	1.72

Thus, S is being delivered in form of a radical on the top atomic layer of Mo, which is continuously losing Se at a very slow etching rate. This will help in formation of bonds

between Mo and S, as the system always tries to achieve a state of maximum stability. Always remember that there is a good competition between the etching rate of top layer and replacement of a new element on it. But since there is a continuous supply of sulfur (in form of H_2S or S gas resulting into S radicals) while the $MoSe_2$ monolayer loses selenium from the top, it maintains the stability of structure and prevents over etching and diffusion of selenium from bottom layer to the top layer. Also, the distance of substrate from the plasma tail must be defined in such a way that the ions that are impacting on the sample are much less than the replacement by new S radicals. But we can never win the game in this battle between etching Se and replacing it with S instantaneously. So, a post thermal sulfurization is required after etching because at the end of plasma processing the sample still has few sites which are being etched by the plasma ions but are not being replaced.

This creates a structure where the top Se layer of $MoSe_2$ is completely stripped off and more than ~98 % of the sites are being replaced by S during plasma processing, while there still can be as many as ~2 % sites which are either weakly bonded with H or the sites are still very active. Thus, this results in a Janus structure of SeMoS but with some defects. To eliminate these defects and crystallize the structure, post sulfurization has to be performed on this Janus structure.

3.6 Sulfurizing into crystalline Janus Se-Mo-S

There can be two ways to sulfurize the samples after plasma stripping process: ex-situ and in-situ. In case of ex-situ sulfurization, the chances of oxidizing the Mo sites can increase if the top layer H bonding is not very stable or if there are still some active sites on top of Mo layer which are not bonded with S during plasma processing.

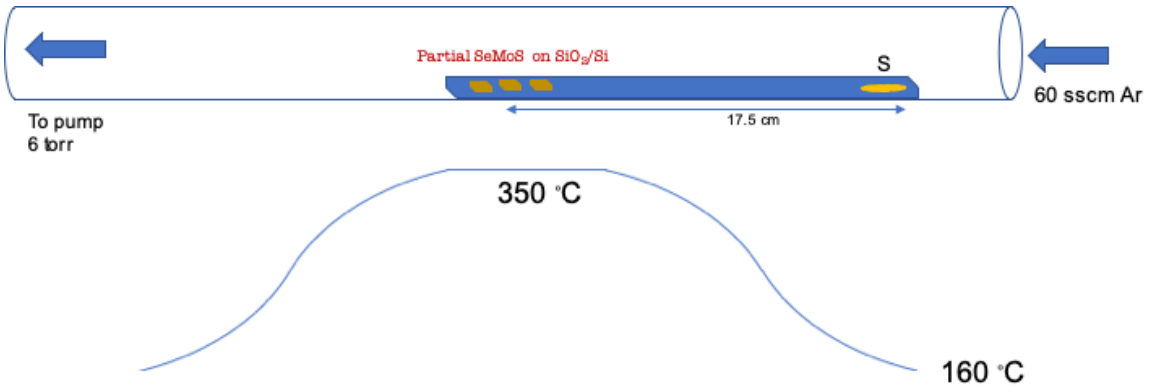

Figure 3.14 Schematic for post thermal in-situ sulfurization for increasing quality of Janus SeMoS after plasma enhanced replacement sulfurization

In case of in-situ process, sulfurization was carried out in the same 1" quartz tube. A metallic (iron) spring was used for pushing the quartz boat containing plasma etched samples and sulfur powder (Sigma-Aldrich, 99.98% purity) inside the furnace region with the help of a magnet from outside of the tube. Sulfur powder was kept approximately 17.5 cm upstream in the same boat from the center sample. The sample was pushed to the center of furnace where the temperature was ramped to 350 ˚C with a rate of 35 ˚C/min while the temperature for S powder simultaneously reaches to 160 ˚C when the center of the furnace reaches at 350 ˚C. Sulfurization was done for 30 min in pure Argon environment with the gas flow rate of Argon gas at 60 sccm. The base pressure was 8 mTorr while the pressure after flowing 60 sccm of argon gas was maintained at 6 Torr with the help of a vacuum pump connected to the downstream side of tube.

Similar parameters were used for the ex-situ sulfurization process in a separate tube with the same dimensions. All the parameter remains the same except that the sample was exposed in ambient gases which may increase the chances of oxidation on top of Mo as discussed before. Further characterization could be done with Raman as conversed in the following section.

3.7 Raman Spectroscopy and Photoluminescence

Raman and PL data were taken with a blue laser (488 nm) with 5 sec of exposure time for 5 accumulations at 5% laser power. These Raman signals can be compared with the DFT calculations as shown in figure 3.15.

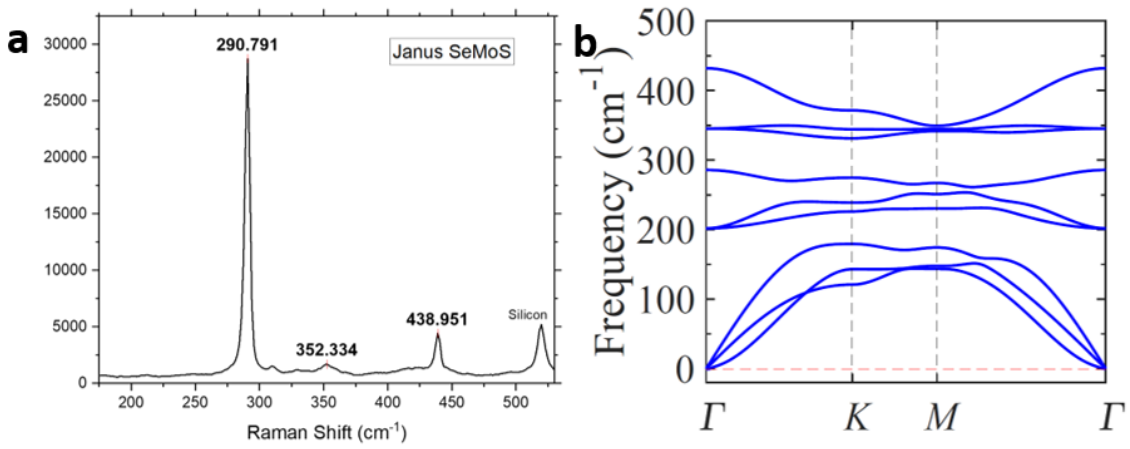

Figure 2.15 (a) Raman signals from Janus SeMoS (b) Phonon dispersion for SeMoS

The intense peak at 290.8 cm^{-1} is an out-of-plane A^1_g mode while a small peak observed at 352.3 cm^{-1} is an in-plane E^1_{2g} mode of vibration. There is also a peak at 438.9 cm^{-1} which is a B^1_{2g} mode of vibration [66] which was observed with this blue laser. But when low energy lasers like green (532 nm) and red (633 nm) laser were used, this peak showed a very diminishing behavior, which indicates that this mode can thus be observed with higher energy laser, but low energy laser might not be capable enough to activate the mode.

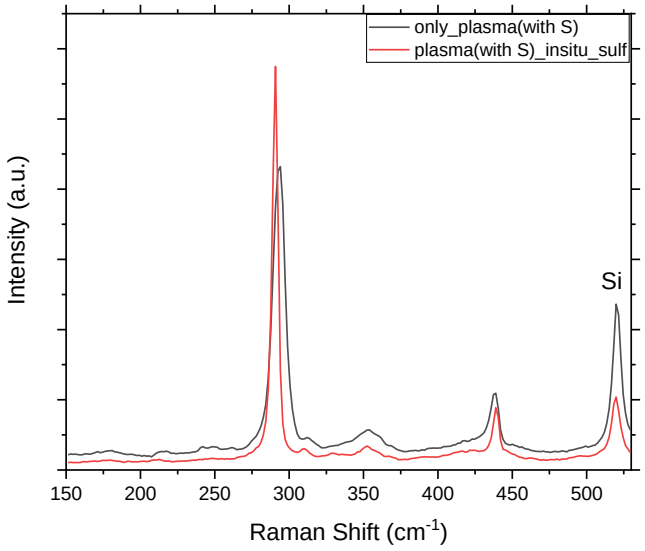

Figure 3.16 Comparing Raman peak's FWHM for only plasma enhanced replacement sulfurization (PERS) SeMoS (black) with the PERS SeMoS after post in-situ sulfurized (red)

The Raman comparison for SeMoS creation without post sulfurization and with post in-situ sulfurization are shown in figure 3.16. The results suggest that the Raman peak broadness of the samples which were sulfurized in-situ when compared with the samples those which were created only during PER differs in the quality by the level of defects. As shown in the Raman plot, the out of plane peak's Full Width Half Max (FWHM) for the sample without post sulfurization is much higher than that of the in-situ sulfurized samples. So, for full replacement of Se with S on the top layer with minimal number of defects, in-situ sulfurization must be adopted. The FWHM of the sample changes from ~7 cm^{-1} for only plasma processed sample to ~3.5 cm^{-1} for a post in-situ sulfurized sample. This shows that a good SeMoS structure can also be created by doing only PER of monolayer MoSe2 even without post sulfurization processing, if the sulfur distance is optimized in such a way that the etching rate of selenium is comparable with the replacement rate of sulfur during PER.

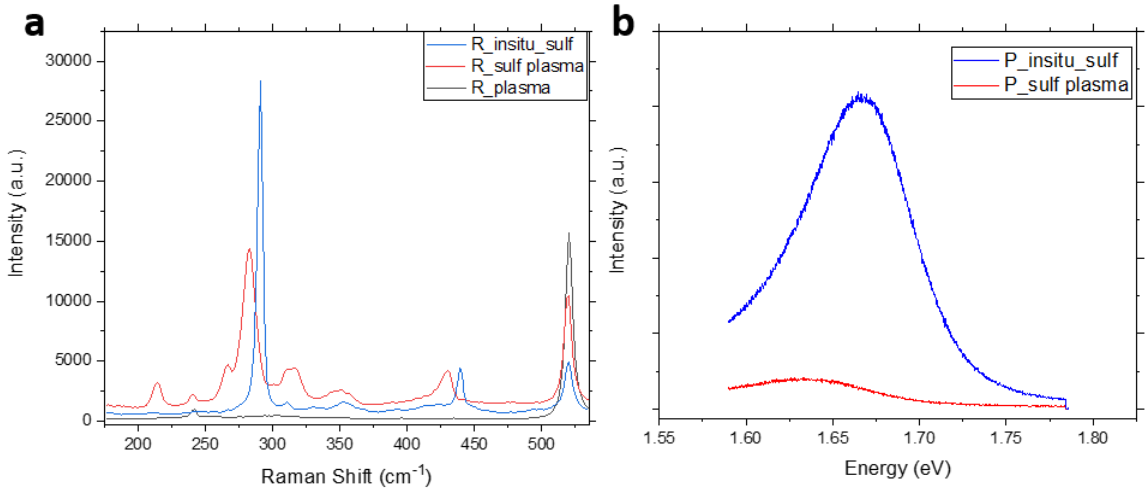

Figure 3.17 (a) Raman comparison for plasma without S (black), PER with incomplete etching (red) and in-situ sulfurized PERS SeMoS (blue) (b) PL comparison for incomplete PERS SeMoS (red) with SeMoS after in-situ sulfurization of PERS SeMoS (blue)

Figure 3.17 (a) indicates a process of transition from the initial stage to a final stage, and how a post in-situ sulfurization is a better option rather than choosing to create a Janus structure only by plasma processing.

Stripping and sulfurization were performed in the same way as mentioned previously while keeping the sample at 3 cm upstream from plasma tail. Black line indicates only plasma stripping without the presence of sulfur, showing diffusion of Se from bottom and generation of small signals for MoSe2. Red line indicates sulfur assisted plasma stripping (PER), showing that if Se is not replaced completely by S during the process then it might show MoSe2 peaks (creating immature Janus structure showing a transition phase) and also the raman signal from SeMoS could move from the gamma point symmetry due to defects (refer phonon dispersion of SeMoS). Blue line indicates sulfur assisted plasma stripping with in-situ sulfurization, showing that a perfect crystalline SeMoS can be created with minimal defects by immediately substituting the defect sites which were casued during PER by post in-situ sulfurization method.

Figure 3.17 (b) shows the photoluminescence (PL) of SeMoS Janus structure measured with a blue laser of 488nm wavelength. The blue line indicates the data taken on the in-situ sulfurized perfect Janus SeMoS for 5 sec laser exposure with 5 accumulations at 5% laser power. The PL peak position was observed to be at 1.67 eV. While the red line indicates the data taken for a sample after incomplete PER in presence of sulfur without in-situ sulfurization indicating the red shift and broadening of PL peak postion due to defects.

3.8 Low temperature Raman and Photoluminescence Spectroscopy

Another set of measurements were taken with a red laser of 633 nm at varying temperatures, ranging from room temperature to as low as 5 K. Figure 3.18 shows the raman signals for SeMoS taken at 5 K.

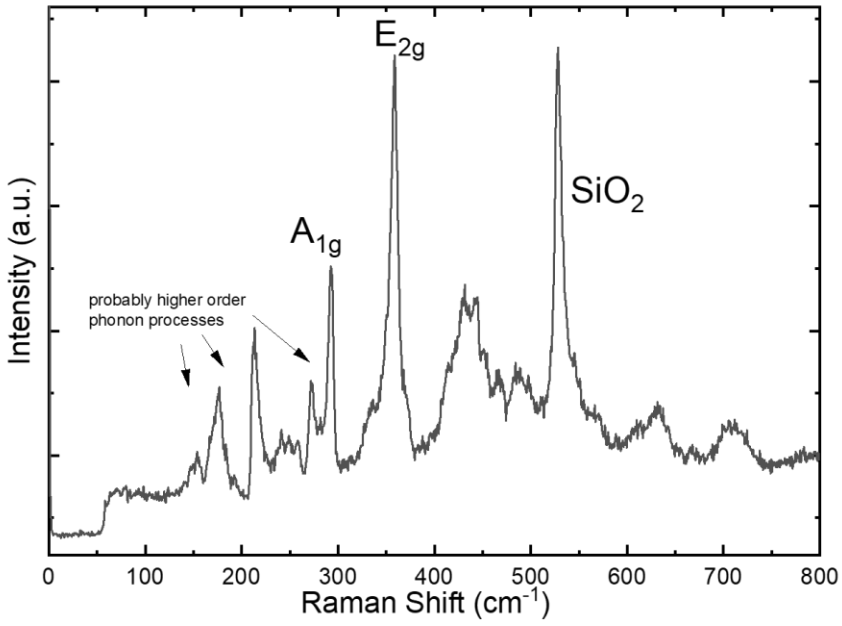

Figure 3.18 Raman for monolayer SeMoS at 5 K

Strong resonant processes could be observed due to excitation with much higher wavelength. Also, at such a low temperatures, defects couldn't play much role so the

vibrations purely comes from the symmetry. Thus sharp peaks could be obseverved and analyzed.

Photoluminescence was performed with the same laser of 633 nm wavelength in a wide range from room temperature to 5 K as showing in figure 3.19.

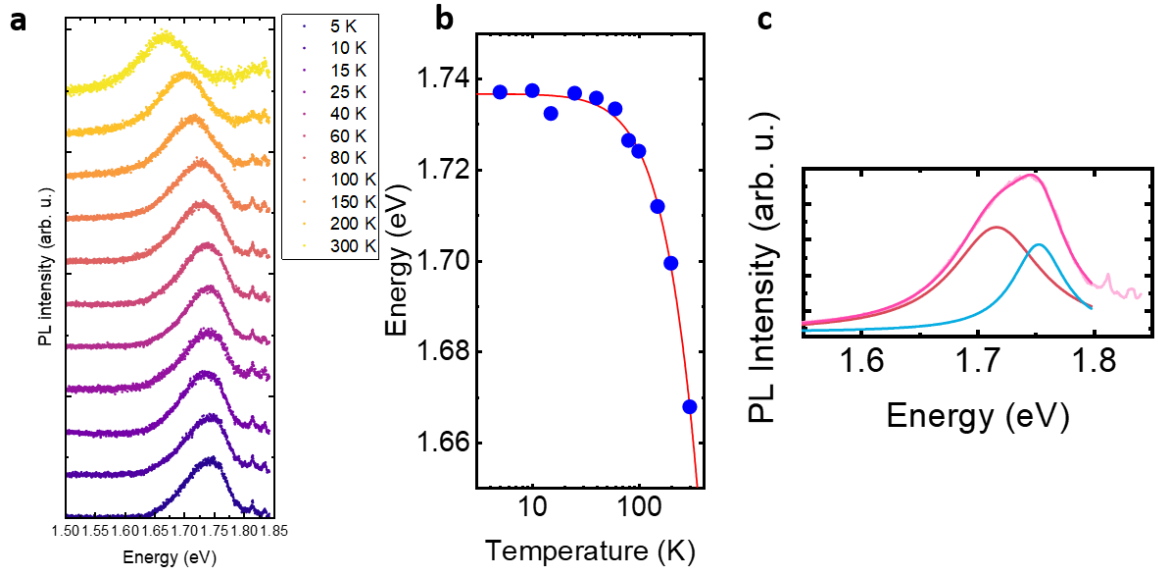

Figure 3.19 (a) Temperature dependent PL for SeMoS (b) Varshni's law curve fitting for low T PL measurement (c) Curve fitting of SeMoS PL peak measured at 5 K

It could be observed from figure 3.19 (a) & (b), when temperature drops down to 5 K the peak position blue shifts from 1.67 eV to ~1.74 eV following a perfect curve fitting according to Varshni's law as mentioned before (eq. 2.1). Also, there is a pretty strong asymmetry in the peak. So, a double Lorentian fit was necessary as shown in figure 3.19 (c), which convolutes two peaks separated by ~35 meV. It is very reasonable to imply this to be splitting of trion and exciton.

A power dependent PL measurement was performed with a similar setup at 10 K. It could be observed from figure 3.20 (a) that there is an increase of PL intensity with increasing incident laser power on the sample. While from figure 3.20 (b) it could be

clearly implied that the log plot of PL Intensity vs Excitation Power is showing a linear characteristics and there is no change of slope for trion and exciton peaks, which indicates that there is no saturation for them even at higher laser power.

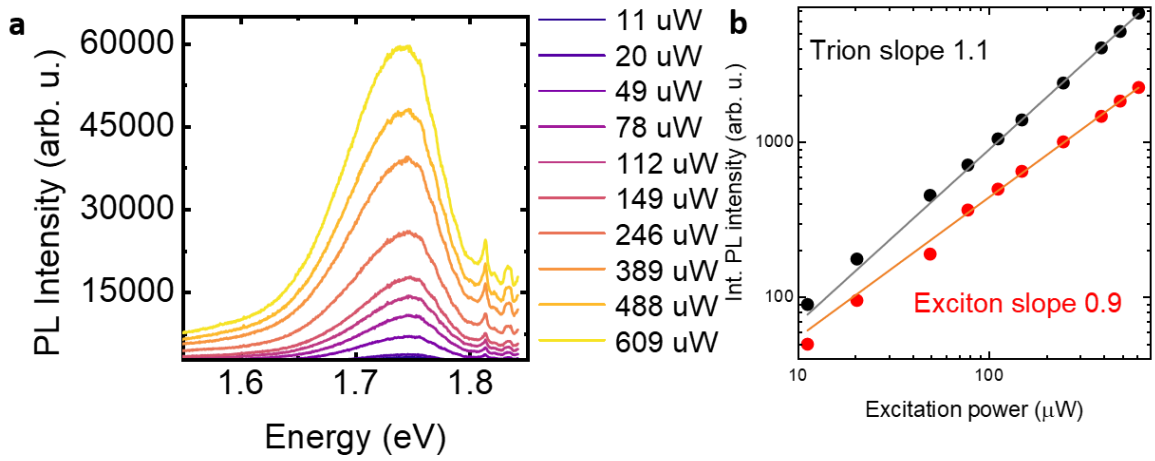

Figure 3.20 (a) Power dependent PL Intensity for SeMoS monolayer with Red Laser (633 nm) (b) Log plot for PL intensity vs Excitation Power

This elucidates that PL is not emerging from a defect site or it could saturate at some point soon with an increase of laser power. Also, a small red shift could be observed with increasing laser power which is an evidence of introduction of defects, but the material is stable enough that it is not getting defected easily.

3.9 Atomic Force Microscopy

Topology and height profile were measured by NT-MDT setup in a non-contact AFM tapping mode. Janus SeMoS monolayer on SiO2/Si substrate was raster scanned with 512-pixel density. It was found that the thickness is still in the monolayer limit.

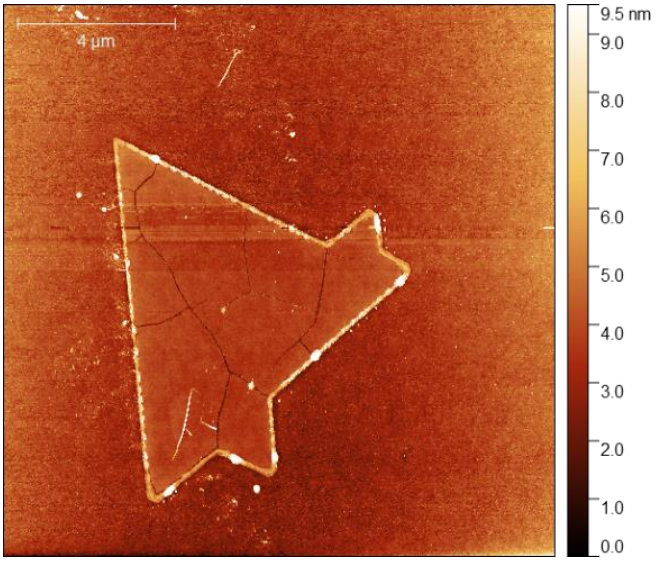

Figure 3.21 Topology of SeMoS by AFM imaging

As it could be observed from this image, cracks would form on monolayer structure while trying to replace a top atomic layer with another, since plasma ions has a very high energy, as it was observed before in case of intense plasma processing. The plasma etching process with hydrogen as a carrier gas acts very gentle but when sulfur reaches near plasma tail, sulfur also undergoes ionization which leads to high impact energies on the flakes. This could result in few cracks which are visible in the AFM imaging as shown in figure 3.21.

If the path for getting Janus SeMoS, started from MoS_2 monolayer instead of $MoSe_2$ monolayer then S must be replaced by Se during PER processing which could result in huge defects or holes in flakes due to ionization of Se (much heavier and thus high impact energies).

Chapter 4 Plasma assisted formation of Janus Se-W-S

4.1 Introduction

Similar process was adopted to another TMDC with selenium as the chalcogenide atom of the structure to claim the repeatability of the developed methodology. CVD grown WSe2 monolayer on sapphire was used as a parent structure (like MoSe2/MoS2) which was then transformed to a Janus structure (SeWS) and characterized. Here also, similar procedure must be followed as the element which is being removed (Se) and the element which has to be introduced (S) into the structure are same as for the case of SeMoS Janus (from MoSe2). Cohesive energy of W with Se is higher compared to Mo with Se [73], [74]. So, care must be taken when considering the stripping process, as it depends on the bonding energies of the parent material (WSe2) that has to be stripped.

4.2 WSe2 characterization

A CVD grown monolayer of WSe2 on sapphire substrate was initially characterized with the help of Raman and PL spectroscopy for identifying the quality.

Raman and PL characterization were performed with the same setup as mentioned for characterizing MoSe2 and SeMoS. Data was collected on the sample with a blue laser of 488 nm wavelength with 5 sec of exposure time. Here, 10% laser power was used with 5 set of accumulations for improving signal to noise ratio.

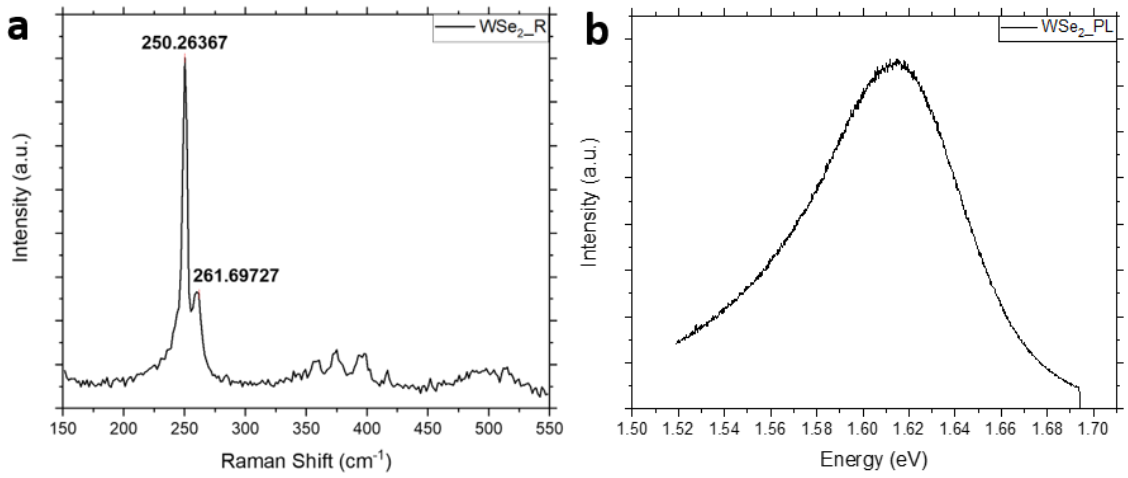

Figure 4.1 (a), (b) Raman and PL for CVD grown WSe2 with Blue Laser (488 nm)

Figure 4.1 (a) shows Raman peak at 250.25 cm^{-1} as an in-plane E^1_{2g} mode and 255.36 cm^{-1} as an out-of-plane A^1_g mode and some other higher order vibration mode. And PL peak position was at ~1.61 eV which is also 500 meV lower than the expected PL peak position, because of the same reason of strain as mentioned for the case of MoSe2 monolayer flakes [76].

4.3 Plasma stripping

Same setup of PER on the upstream side of an ICP plasma setup was carried out to strip and replace the top layer of Se from monolayer WSe2 and replace it with S during the stripping process followed by a post in-situ thermal sulfurization to crystalize the structure of SeWS with better crystallinity and high quality with minimal defects. PER was carried out by flowing H2 as a carrier gas at a flow rate of 20 sccm for generation of plasma. The pressure was maintained at 294 mTorr with the help of a vacuum pump and RF power of 15 W was applied from a RF source to a helical shaped copper coil (with five turns), wound on the quartz tube. As the cohesive energies of WSe2 is higher than MoSe2, the time of stripping the top layer has to be increased to 15 min because it would take longer time to

strip Se, as the bonding between W with Se is stronger than Mo with Se. The pressure during the PER process was maintained at 294 mTorr and the sample distance from the plasma tail was changed from 3 cm (for MoSe2) to 2 cm in case of WSe2 stripping while keeping the distance of S from plasma tail end to be 20.5 cm while applying 15 W power from an RF source.

4.4 Sulfurization into Janus SeWS

Post in-situ sulfurization was carried out in the same setup of PER process to avoid any oxide formation on W active sites. Since the energy required for bond formation W with S is higher that Mo with S, the temperature and pressure during sulfurization must be optimized accordingly.

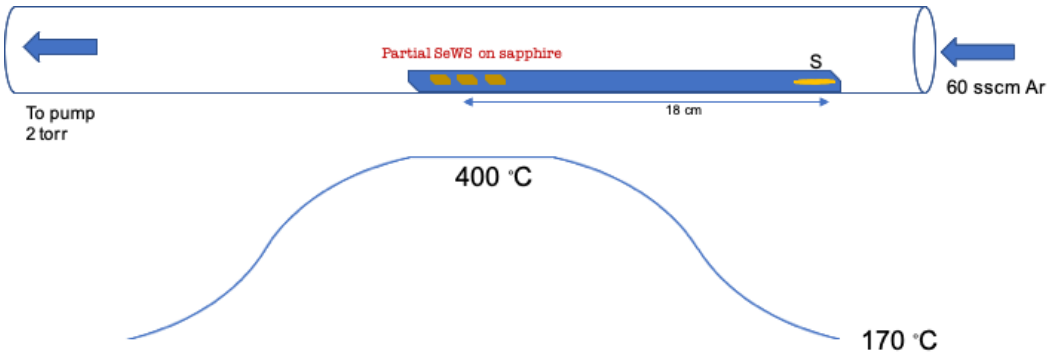

Figure 4.2 Schematic for post in-situ sulfurization of PERS SeWS

For sulfurization in Ar environment, sample has to be pushed into the center of the furnace heating zone, where the temperature of sample is ramped to 400 ˚C while S must be kept 18 cm upstream from the sample where the temperature reached 170 ˚C. The pressure must be maintained at 2 Torr with a constant Argon gas flow rate of 60 sccm during the sulfurization period of 30 min. After allowing the sample to cool down naturally to room temperature, the sample was taken out for further characterization.

4.5 Raman characterization

Raman was measured with the same setup and parameters as for WSe2 for a better comparison.

The new emerging peaks of Janus SeWS were observed to be at 284.51 cm^{-1} and 333.18 cm^{-1} which could be further verified from 1st principle DFT calculations of phonon dispersion as shown in figure 4.3. The peak at 284.51 cm^{-1} is an out-of-plane A^1_g mode of vibration while a peak at 333.18 cm^{-1} is an in-plane E^1_{2g} mode of vibration [80].

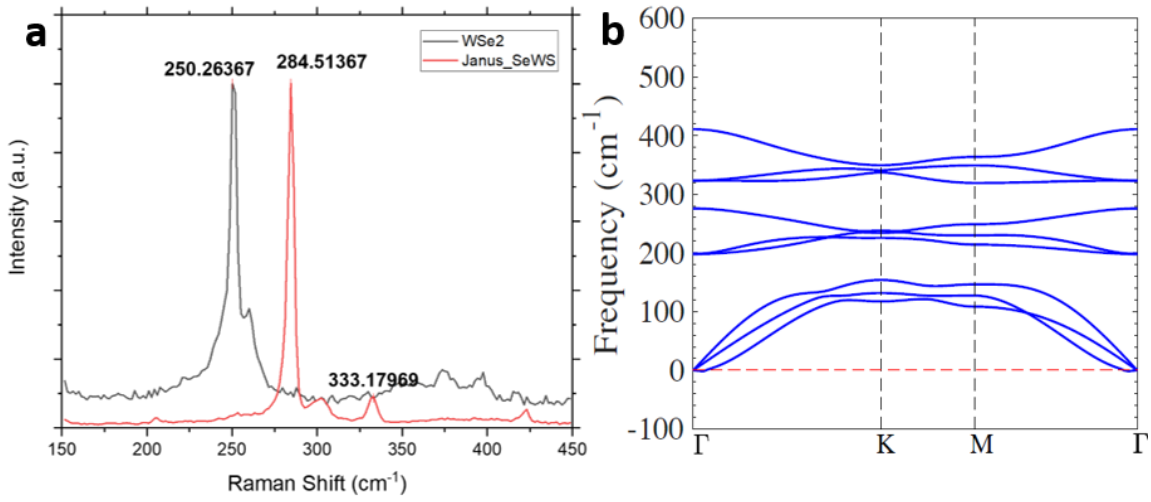

Figure 4.3 (a) Raman comparison of WSe2 (black) with Janus SeWS (Red) (b) Phonon dispersion for SeWS

The FWHM of A1g mode of this new SeWS structure was even smaller than that of the actual WSe2 growth dictating a very superior quality Janus structure creation could be achieved if the parameters are optimized accordingly.

The effects of distance of sample from the plasma tail end, and the effects of duration of PER process accounts to be one of the major criteria for deciding the quality of new emerging structure with a replaced top atomic layer. Few experiments were carried out to determine optimum parameters for obtaining perfect crystalline Janus SeWS from

a CVD grown WSe2 monolayers. Figure 4.4 shows the effect of etching time and distance of plasma tail end from WSe2 sample during PER on WSe2 monolayers with in-situ post sulfurization. In figure 4.4, a Raman plot in red is shown for a sample kept at 3 cm away from the plasma tail end, indicating a shoulder of out-of-plane vibration mode of WSe2 structure which further implies under-stripping of top atomic layer of Se from the parent structure due to less time of etching.

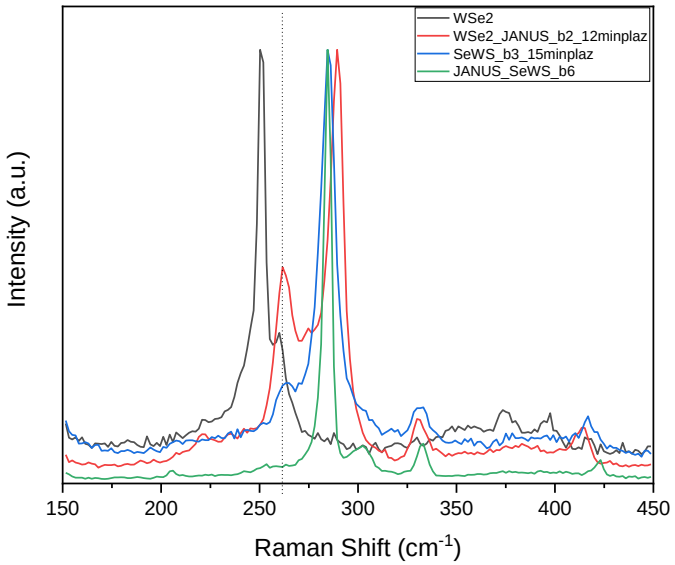

Figure 4.4 Comparison between Raman of monolayer WSe2 (black), 12 min PER for WSe2 (red) at 3 cm, 15 min PER for WSe2 at 3 cm (blue) and 15 min PER for WSe2 at 2 cm (green)

Similar behavior was observed when stripping was done for 15 min instead of 12 min by keeping the sample distance same as before (3 cm from plasma tail end) (blue). Since stripping and replacement was done for a longer time, the shoulder from parent structure was significantly reduced in intensity but still visible, which makes the sample not a complete SeWS structure. To avoid that incomplete etching, the sample was pushed near plasma tail end and now the sample was 2 cm from plasma tail end for 15 min of PER, which is shown by a green line in Raman plot.

4.6 Comparison of Janus

Numerous comparisons based on Janus of SeMoS and SeWS could be done for a better understanding of emergence of Raman and pl signals based on their atomic sizes and weights. Also, it has been compared with the alloyed structures of MoSSe and WSSe with different atomic ratios of S and Se which can be called a randomized Janus. Alloys have a random (mixed) placement of S and Se throughout the structure, which is not helpful in creating a polar material.

4.6.1 Parent structures

A simple comparison was carried out for both the Janus samples of SeMoS and SeWS with their parent structures of MoSe2/MoS2 and WSe2/WS2 respectively.

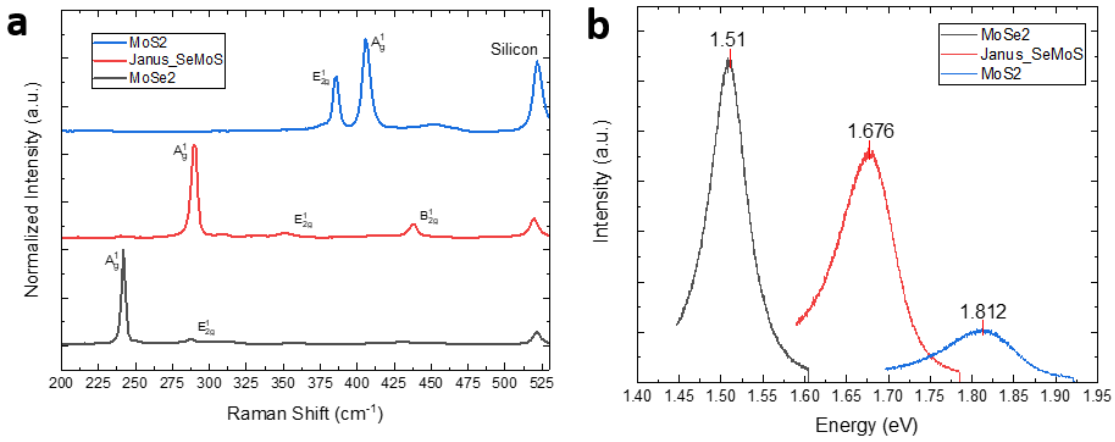

Figure 4.5 (a), (b) Raman and PL peak comparison of MoSe2 (black), SeMoS (red) and MoS2 (blue) measured with same parameters

For the group of MoSe2, SeMoS and MoS2 monolayer samples, all the Raman and pl measurements were carried out with a blue laser of 488 nm wavelength incident at 5% laser power for 5 sec of exposure time with 5 set of accumulations. While for the case of WSe2, SeWS and WS2 group, the laser power used was 10% with 5 sec exposure time for 5 set of accumulations.

Figure 4.5 shows a comparison of Raman and pl for CVD grown MoSe2, MoS2 with Janus SeMoS, while figure 4.6 shows the comparison of CVD grown WSe2, WS2 with Janus SeWS. Raman and pl signals of the obtained Janus structure are in between their respective parent structures. PL Intensities and FWHM of Janus structure are also comparable with their parent structures when the data was collected with the same setup and parameters.

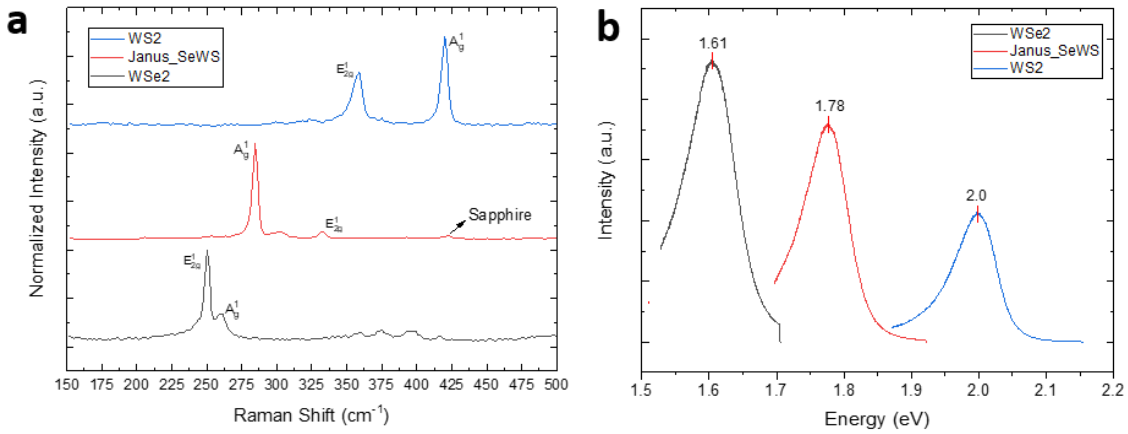

Figure 4.6 (a), (b) Raman and PL peak comparison of WSe2 (black), SeWS (red) and WS2 (blue) measured with same parameters

It could thus be stated that the Raman vibration modes are shifting from lower frequency to higher frequency when going from structure having only Se to the structure having only S in it. The PL peak position of new Janus structure is in between their parent structures as expected [65], [80].

4.6.2 Degree of stripping and sulfurization based on sample position

Plasma enhanced replacement (PER) with S and post in-situ sulfurization was carried out on 3 samples of MoSe2 with same plasma parameters but kept at varying distances upstream from the plasma tail end.

In figure 4.7, the degree of stripping and sulfurization of the sample with respect to the distance of sample from the plasma tail is depicted. The sample which was closest to the plasma tail end gets completely etched with a very strong signal coming from SeMoS Janus structure while with increasing the distance of sample from the plasma tail end, there was an emergence of shoulder on left (lower frequency), coming from the parent structure of MoSe2. Also, a shift in the out-of-plane SeMoS peak to lower frequencies was observed as we go away from upstream plasma tail end which is an indication of incomplete etching of MoSe2 flake. So, there are also some top layer Se sites (heavy atom) bonded with Mo which is dampening the higher frequency of vibration caused from the bond of S atoms (lighter atom). This can also be an effect of defects in SeMoS structure which could cause Raman signals to arise away from gamma symmetry point as discussed before.

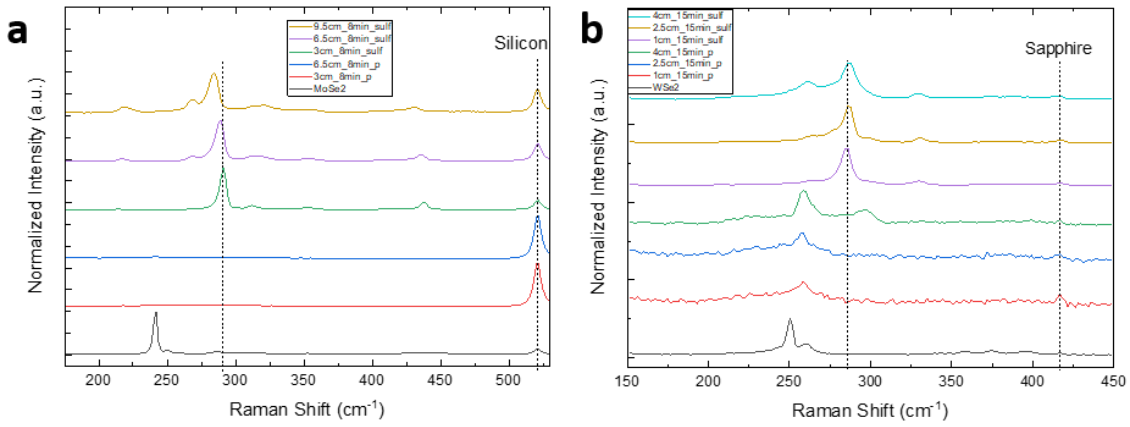

Figure 4.7 (a) Raman signals for MoSe2 (black), only plasma etched (without S) (red&blue) and for in-situ sulfurized PER SeMoS (green,purple&yellow) (b) Raman signals for WSe2 (black), only plasma etched (without S) (red,blue&green) and for in-situ sulfurized PER SeWS (purple,yellow&cyan)

These kind of results were also consistent with SeWS Janus as shown in figure 4.7 (b), where the bottom line shows the parent structure of WSe2 and then moving up in the

graph the next three are just plasma stripped samples without sulfur presence and sulfurization, while the top three are the samples kept at same distances as the last time of only plasma stripping but the only changes were that this time there was PER of sulfur and also in-situ sulfurization was performed.

4.6.3 Alloy comparison

Alloy comparison was performed on exfoliated CVT (Chemical Vapor Transport) grown samples to verify the differences in perfect Janus structure with the randomized placement of S and Se in different atomic ratios. It could be observed from Raman signals of alloy of MoSSe with different atomic ratios of S and Se ($MoS_{1.7}Se_{0.3}$, $MoS_{1.5}Se_{0.5}$ and $MoS_{1.3}Se_{0.7}$) from figure 4.8 (a), that the peaks observed from alloyed structure is very different from the peaks observed from a Janus structure of SeMoS. This indicates that there is no randomized formation of alloying in this process of plasma enhanced replacement.

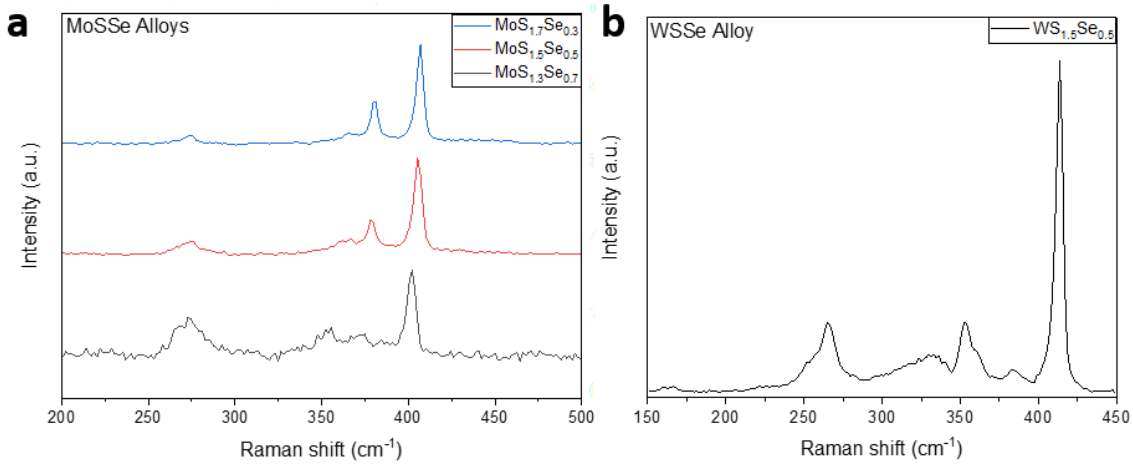

Figure 4.8 (a) Raman signals for alloy of MoSSe (b) Raman signals for alloy of WSSe

It was also evident from the Raman signals of alloyed WSSe ($WS_{1.5}Se_{0.5}$) that Janus SeWS created from the developed methodology does not promote any kind of alloy formation but only a highly crystalline Janus structure with a perfect polar nature.

Chapter 5 CONCLUSION AND FUTURE DIRECTIONS

5.1 Introduction

Till date, extensive theoretical studies have been done on various aspects of Janus TMDCs, but due to certain limitations of previous studies to effectively create a highly crystalline Janus structure, these exciting properties remained experimentally unknown. A full potential of polar 2D materials can now be explored by creating variety of highly crystalline Janus TMDC structures by using the innovative methodology presented in this work.

A critical aspect and one of the key innovations of this methodology is the ability to synthesize large-area and highly crystalline 2D Janus layers without alloying them. Energetically, it is rather easy to alloy different chalcogens to form 2D alloys as it has been conventionally done by many research groups. This innovation will enable researchers to probe quantum effects arising from 2D Janus layers without any ambiguity.

5.2 Conclusion

For establishing a better control over the parameters for Plasma Enhanced Replacement of new elements in future, there are few aspects that needs to be emphasized as reflected below:

- The level of defects generated during the process of plasma enhanced replacement (PER) can be controlled by controlling the plasma parameters and thus improving the overall efficiency of getting a high-quality crystal with minimum defects.
- The introduction of defects is more likely to be expected when the distance of sample and the new element is not optimized properly (with respect to

the coil or plasma tail end) such that the etching rate of parent structure is much higher than the replacement rate of the new element into the structure.

- Plasma etching rate increases with the increase of atomic weight of the carrier gas, because the bombardment of heavier atom can displace or break the bonds and atomic sites very effectively. Thus, when an atom of much heavier atomic weight needs to be incorporated by replacing previous surface atomic site, then the pressure and gas flow rate inside the chamber must be raised optimally, at the same time also controlling the other plasma parameters thus increasing the ion-scattering and thereby reducing the impact energy of the ions being bombarded.
- Higher flow rate increases the density of plasma up to a certain limit, but after a threshold it would reduce the energy of plasma due to scattering and at the same time it would be helpful in reducing the impact energy of the ions on the sample, resulting into more gentle stripping and replacement.
- As in the case of Se replaced by S (for this specific work demonstrated), when we move the Sulfur position away from plasma tail end (or coil) on the upstream side, the transfer of Sulfur on the sample reduces because the effect of magnetic field strength weakens as we move far from the coil. This weakening of magnetic field directly affects the electrical field generated in that region which leads to reduction in acceleration of electrons and thus decreases ionization and dissociation of hydrogen gas molecules. Consequently, this lessens the concentration of hydrogen ions and hydrogen radicals which eventually affects the amount of S radicals at the

sample (substrate) site because of less amount of S getting knocked from the sulfur source.

- The application of this innovation will not be limited to replacing Se (one chalcogen) atomic layer with S atoms (another chalcogen), but it could also be adopted in future for functionalizing the surface by different elements without altering the parent crystal structure. Though care must be taken when trying to incorporate heavy elements on to the parent structure.

A path for SeMoS/SeWS generation could also start from a CVD MoS2/WS2 monolayer. But, while going from MoS2/WS2 to SeMoS/SeWS instead of MoSe2/WSe2 to SeMoS/SeWS, the pressure and gas flow rate of the system should be increased and manipulated accordingly because when Se atom gets ionized and accelerated, they would etch away the whole structure or could create holes into the monolayer structure because of higher atomic size (weight).

Using the established growth process, we may continue to improve the crystal quality of 2D Janus crystals throughout the family to Janus TMDC by optimally playing with the parameters of plasma during the plasma enhanced replacement process. To further improve the crystallinity, it is advisable to determine the lowest possible plasma power required to strip-off the top atomic (chalcogen) layer in order to minimize plasma induced defects. This versatile technique is flexible enough to synthesize other yet-to-be-discovered 2D Janus crystals.

In this methodology, choosing the carrier gas for plasma generation and transferring of required new material on top of a parent structure also plays a major role in functionalizing the surface. It can thus be concluded that this method could be adopted for any kind of surface functionalization procedures in future.

5.3 Future directions

Intense theoretical studies are needed which could help to simulate the plasma properties at a larger extent, such as the induced magnetic field and electrical field from the coil which could eventually be helpful in determining the extent of ionization and dissociation based on the energy generated with respect to distance from coil. This will thus be helpful in deciding an ideal position for the sample which has to be etched and also the element which must be replaced during the entire process. More efforts must be laid towards the actual kinetics of the mechanism proposed to firm up the conclusions.

Optimum control over the plasma parameters for different set of element's replacements could be worked out by starting the PER process from a parent structure with different top atomic layer. Preliminary efforts have already been made on creating SMoTe Janus structure with the help of this PER process with an added post in-situ thermal tellurization, however, it requires better control over the plasma parameters. Replacement of surface atomic layer for 2D materials with different crystal structures like InSe or GaSe should also be considered in future.

As discussed before about the theoretical studies and predications made for room temperature ferromagnetism, there could be an opportunity to create a room temperature ferromagnet which an intrinsic electrical field in a monolayer dimension.

Janus materials could thus be helpful in exploring rich quantum physics which is still unknow to the date. There could now be a possibility to experimentally evidence Rashba splitting by adopting various characterization techniques for these Janus materials. Hetero and Homo structures made out of different Janus structures could begin a potential field of piezoelectricity which could create a huge impact for technological advancements in industries.

Since PER is a room temperature mechanism, it is majorly driven by the kinetics of the process. This innovative methodology of plasma enhanced replacement could easily be adopted to industrial standards since the developed process has minimal contamination due to in-situ processing. Also, there is an added advantage that the process of plasma enhanced replacement consumes a very small quantity of precursor (element which has to be replaced) during the whole process thus resulting into minimal wastage of the element. The process is accomplished in a very short duration of time making it a very fast and effective processing technique for creating a greater quality crystal with minimal loss and thus a very cost-effective methodology.

The avenues mentioned is just a bucket from an ocean while there is much more to be explored from the developed methodology and Janus structures.

REFERENCES

[1] W. F. Brinkman, D. E. Haggan, and W. W. Troutman, "History Transistor," *IEEE J. Solid-State Circuits*, vol. 32, no. 12, pp. 1858–1865, 1997.

[2] 1 K. S. Novoselov,1 A. K. Geim *et al.*, "Electric Field Effect in Atomically Thin Carbon Films," *Science (80-.).*, vol. 306, no. October, pp. 666–669, 2004.

[3] A. K. Geim and K. S. Novoselov, "The rise of graphene," *Nat. Mater.*, vol. 6, p. 183, Mar. 2007.

[4] C. Lee, X. Wei, J. W. Kysar, and J. Hone, "of Monolayer Graphene," *Science*, vol. 321, no. July, pp. 385–388, 2008.

[5] S. Stankovich *et al.*, "Graphene-based composite materials," *Nature*, vol. 442, no. 7100, pp. 282–286, 2006.

[6] A. H. Castro Neto, F. Guinea, N. M. R. Peres, K. S. Novoselov, and A. K. Geim, "The electronic properties of graphene," *Rev. Mod. Phys.*, vol. 81, no. 1, pp. 109–162, 2009.

[7] S. W. Ng, N. Noor, and Z. Zheng, "Graphene-based two-dimensional Janus materials," *NPG Asia Mater.*, vol. 10, no. 4, pp. 217–237, 2018.

[8] J. O. Sofo, A. S. Chaudhari, and G. D. Barber, "Graphane: A two-dimensional hydrocarbon," *Phys. Rev. B - Condens. Matter Mater. Phys.*, vol. 75, no. 15, pp. 1–4, 2007.

[9] J. Zhou, Q. Wang, Q. Sun, X. S. Chen, Y. Kawazoe, and P. Jena, "Ferromagnetism in semihydrogenated graphene sheet," *Nano Lett.*, vol. 9, no. 11, pp. 3867–3870, 2009.

[10] M. Yang, L. Zhou, J. Wang, Z. Liu, and Z. Liu, "Evolutionary chlorination of graphene: From charge-transfer complex to covalent bonding and nonbonding," *J. Phys. Chem. C*, vol. 116, no. 1, pp. 844–850, 2012.

[11] K. F. Mak, C. Lee, J. Hone, J. Shan, and T. F. Heinz, "Atomically thin MoS2: A new direct-gap semiconductor," *Phys. Rev. Lett.*, vol. 105, no. 13, pp. 2–5, 2010.

[12] A. Splendiani *et al.*, "Emerging photoluminescence in monolayer MoS 2," *Nano Lett.*, vol. 10, no. 4, pp. 1271–1275, 2010.

[13] J. A. Wilson and A. D. Yoffe, *The transition metal dichalcogenides discussion and interpretation of the observed optical, electrical and structural properties*, vol. 18. 1969.

[14] S. Manzeli, D. Ovchinnikov, D. Pasquier, O. V Yazyev, and A. Kis, "2D Transition metal dichalcogenides Strano.pdf," *Nat. Rev. Mater.*, vol. 2, p. 17033, Jun. 2017.

[15] S. Manzeli, D. Ovchinnikov, D. Pasquier, O. V Yazyev, and A. Kis, "2D transition metal dichalcogenides," *Nat. Rev. Mater.*, vol. 2, p. 17033, Jun. 2017.

[16] "Physical properties of layer structures : optical properties and photoconductivity of thin crystals of molybdenum disulphide," *Proc. R. Soc. London. Ser. A. Math.*

Phys. Sci., vol. 273, no. 1352, pp. 69–83, 1963.

[17] R. F. Frindt *et al.*, "Exfoliated MoS2 monolayers as substrates for magnetic materials," *J. Appl. Phys.*, vol. 70, no. 10, pp. 6224–6226, 1991.

[18] U. Stuttgart, "Epitaxial growth of coronene and hexa-peri-benzocoronene on MoS2(0001) and graphite (0001).pdf," vol. 268, pp. 296–306, 1992.

[19] Y. Iwakabe, M. Hara, K. Kondo, S. Oh-Hara, A. Mukoh, and H. Sasabe, "Anchoring structure of binary mixture of liquid crystals studied by scanning tunneling microscopy," *Jpn. J. Appl. Phys.*, vol. 31, no. 12, pp. L1771–L1774, 1992.

[20] A. Manivannan *et al.*, "Scanning probe microscopic investigation of epitaxially grown c 60 film on mos2," *Jpn. J. Appl. Phys.*, vol. 31, no. 11 R, pp. 3680–3685, 1992.

[21] G. E. Collins *et al.*, " Orientation and structure of monolayer →→ multilayer phthalocyanine thin films on layered semiconductor (MoS 2 and SnS 2) surfaces ," *J. Vac. Sci. Technol. A Vacuum, Surfaces, Film.*, vol. 10, no. 4, pp. 2902–2912, 2002.

[22] A. M. Van Der Zande *et al.*, "Grains and grain boundaries in highly crystalline monolayer molybdenum disulphide," *Nat. Mater.*, vol. 12, no. 6, pp. 554–561, 2013.

[23] T. Habe and M. Koshino, "Spin-dependent refraction at the atomic step of transition-metal dichalcogenides," *Phys. Rev. B - Condens. Matter Mater. Phys.*, vol. 91, no. 20, pp. 1–5, 2015.

[24] A. Pulkin and O. V. Yazyev, "Spin- and valley-polarized transport across line defects in monolayer MoS2," *Phys. Rev. B*, vol. 93, no. 4, pp. 1–5, 2016.

[25] B. Radisavljevic and A. Kis, "Mobility engineering and a metal–insulator transition in monolayer MoS2," *Nat. Mater.*, vol. 12, p. 815, Jun. 2013.

[26] Z. Guan, S. Ni, and S. Hu, "Tunable Electronic and Optical Properties of Monolayer and Multilayer Janus MoSSe as a Photocatalyst for Solar Water Splitting: A First-Principles Study," *J. Phys. Chem. C*, vol. 122, no. 11, pp. 6209–6216, 2018.

[27] F. Li and Y. Li, "Band gap modulation of Janus graphene nanosheets by interlayer hydrogen bonding and the external electric field: A computational study," *J. Mater. Chem. C*, vol. 3, no. 14, pp. 3416–3421, 2015.

[28] N. C. Frey, A. Bandyopadhyay, H. Kumar, B. Anasori, Y. Gogotsi, and V. B. Shenoy, "Surface-Engineered MXenes: Electric Field Control of Magnetism and Enhanced Magnetic Anisotropy," *ACS Nano*, vol. 13, no. 3, pp. 2831–2839, 2019.

[29] A. C. Riis-Jensen, M. Pandey, and K. S. Thygesen, "Efficient Charge Separation in 2D Janus van der Waals Structures with Built-in Electric Fields and Intrinsic p-n Doping," *J. Phys. Chem. C*, vol. 122, no. 43, pp. 24520–24526, 2018.

[30] Dimple, N. Jena, A. Rawat, R. Ahammed, M. K. Mohanta, and A. De Sarkar, "Emergence of high piezoelectricity along with robust electron mobility in Janus structures in semiconducting Group IVB dichalcogenide monolayers," *J. Mater. Chem. A*, vol. 6, no. 48, pp. 24885–24898, 2018.

[31] D. Er, H. Ye, N. C. Frey, H. Kumar, J. Lou, and V. B. Shenoy, "Prediction of Enhanced Catalytic Activity for Hydrogen Evolution Reaction in Janus Transition Metal Dichalcogenides," *Nano Lett.*, vol. 18, no. 6, pp. 3943–3949, 2018.

[32] H. Jin, T. Wang, Z. R. Gong, C. Long, and Y. Dai, "Prediction of an extremely long exciton lifetime in a Janus-MoSTe monolayer," *Nanoscale*, vol. 10, no. 41, pp. 19310–19315, 2018.

[33] J. Wang *et al.*, "Intriguing electronic and optical properties of two-dimensional Janus transition metal dichalcogenides," *Phys. Chem. Chem. Phys.*, vol. 20, no. 27, pp. 18571–18578, 2018.

[34] J. Liu and S. T. Pantelides, "Mechanisms of Pyroelectricity in Three- and Two-Dimensional Materials," *Phys. Rev. Lett.*, vol. 120, no. 20, p. 207602, 2018.

[35] C. Zhang, Y. Nie, S. Sanvito, and A. Du, "First-Principles Prediction of a Room-Temperature Ferromagnetic Janus VSSe Monolayer with Piezoelectricity, Ferroelasticity, and Large Valley Polarization," *Nano Lett.*, vol. 19, pp. 1366–1370, 2019.

[36] J. Yang, A. Wang, S. Zhang, J. Liu, Z. Zhong, and L. Chen, "Coexistence of piezoelectricity and magnetism in two-dimensional vanadium dichalcogenides," *Phys. Chem. Chem. Phys.*, vol. 21, no. 1, pp. 132–136, 2019.

[37] Y. Wang, W. Wei, B. Huang, and Y. Dai, "The mirror asymmetry induced nontrivial properties of polar WSSe/MoSSe heterostructures," *J. Phys. Condens. Matter*, vol. 31, no. 12, 2019.

[38] Y. Chen, J. Liu, J. Yu, Y. Guo, and Q. Sun, "Symmetry-breaking induced large piezoelectricity in Janus tellurene materials," *Phys. Chem. Chem. Phys.*, vol. 21, no. 3, pp. 1207–1216, 2019.

[39] W. Shi and Z. Wang, "Mechanical and electronic properties of Janus monolayer transition metal dichalcogenides," *J. Phys. Condens. Matter*, vol. 30, no. 21, 2018.

[40] R. Peng, Y. Ma, S. Zhang, B. Huang, and Y. Dai, "Valley Polarization in Janus Single-Layer MoSSe via Magnetic Doping," *J. Phys. Chem. Lett.*, vol. 9, no. 13, pp. 3612–3617, 2018.

[41] Y. C. Cheng, Z. Y. Zhu, M. Tahir, and U. Schwingenschlögl, "Spin-orbit–induced spin splittings in polar transition metal dichalcogenide monolayers," *EPL (Europhysics Lett.*, vol. 102, no. 5, p. 57001, Jun. 2013.

[42] S. Yuan, H. Ding, J. Wang, and Z. Chen, "Extraordinary Magnetoresistance in Janus Monolayer MoTeB 2 : A Theoretical Prediction," *J. Phys. Chem. C*, vol. 122, no. 49, pp. 28423–28430, 2018.

[43] L. Hu and D. Wei, "Janus Group-III Chalcogenide Monolayers and Derivative Type-II Heterojunctions as Water-Splitting Photocatalysts with Strong Visible-Light Absorbance," *J. Phys. Chem. C*, vol. 122, no. 49, pp. 27795–27802, 2018.

[44] X. Tang *et al.*, "Distorted Janus Transition Metal Dichalcogenides: Stable Two-Dimensional Materials with Sizable Band Gap and Ultrahigh Carrier Mobility," *J. Phys. Chem. C*, vol. 122, no. 33, pp. 19153–19160, 2018.

[45] Z. Wang, "2H → 1T′ phase transformation in Janus monolayer MoSSe and MoSTe: an efficient hole injection contact for 2H-MoS2," *J. Mater. Chem. C*, vol. 6, no. 47, pp. 13000–13005, 2018.

[46] H. D. Bui, H. R. Jappor, and N. N. Hieu, "Tunable optical and electronic properties of Janus monolayers Ga2SSe, Ga2STe, and Ga2SeTe as promising candidates for ultraviolet photodetectors applications," *Superlattices Microstruct.*, vol. 125, no. September 2018, pp. 1–7, 2019.

[47] P. Zhao, Y. Liang, Y. Ma, B. Huang, and Y. Dai, "Janus chromium dichalcogenide monolayers with low carrier recombination for photocatalytic overall water-splitting under infrared light," *J. Phys. Chem. C*, vol. 123, no. 7, pp. 4186–4192, 2019.

[48] Y. Bai, Q. Zhang, N. Xu, K. Deng, and E. Kan, "The Janus structures of group-III chalcogenide monolayers as promising photocatalysts for water splitting," *Appl. Surf. Sci.*, vol. 478, no. December 2018, pp. 522–531, 2019.

[49] W. Chen, X. Hou, X. Shi, and H. Pan, "Two-Dimensional Janus Transition Metal Oxides and Chalcogenides: Multifunctional Properties for Photocatalysts, Electronics, and Energy Conversion," *ACS Appl. Mater. Interfaces*, vol. 10, no. 41, pp. 35289–35295, 2018.

[50] Z.-K. Tang, B. Wen, M. Chen, and L.-M. Liu, "Janus MoSSe Nanotubes: Tunable Band Gap and Excellent Optical Properties for Surface Photocatalysis," *Adv. Theory Simulations*, vol. 1, no. 10, p. 1800082, 2018.

[51] X. Ma, X. Wu, H. Wang, and Y. Wang, "A Janus MoSSe monolayer: A potential wide solar-spectrum water-splitting photocatalyst with a low carrier recombination rate," *J. Mater. Chem. A*, vol. 6, no. 5, pp. 2295–2301, 2018.

[52] R. Peng, Y. Ma, B. Huang, and Y. Dai, "Two-dimensional Janus PtSSe for photocatalytic water splitting under the visible or infrared light," *J. Mater. Chem. A*, vol. 7, no. 2, pp. 603–610, 2019.

[53] Y. F. Luo, Y. Pang, M. Tang, Q. Song, and M. Wang, "Electronic properties of Janus MoSSe nanotubes," *Comput. Mater. Sci.*, vol. 156, no. August 2018, pp. 315–320, 2019.

[54] S. Zhang *et al.*, "MoSSe nanotube: a promising photocatalyst with an extremely long carrier lifetime," *J. Mater. Chem. A*, vol. 7, no. 13, pp. 7885–7890, 2019.

[55] F. Li, W. Wei, H. Wang, B. Huang, Y. Dai, and T. Jacob, "Intrinsic Electric Field-Induced Properties in Janus MoSSe van der Waals Structures," *J. Phys. Chem. Lett.*, vol. 10, no. 3, pp. 559–565, 2019.

[56] T. Hu, F. Jia, G. Zhao, J. Wu, A. Stroppa, and W. Ren, "Intrinsic and anisotropic Rashba spin splitting in Janus transition-metal dichalcogenide monolayers," *Phys. Rev. B*, vol. 97, no. 23, pp. 1–6, 2018.

[57] F. Li, W. Wei, P. Zhao, B. Huang, and Y. Dai, "Electronic and Optical Properties of Pristine and Vertical and Lateral Heterostructures of Janus MoSSe and WSSe," *J. Phys. Chem. Lett.*, vol. 8, no. 23, pp. 5959–5965, 2017.

[58] R. Li, Y. Cheng, and W. Huang, “Recent Progress of Janus 2D Transition Metal Chalcogenides: From Theory to Experiments,” *Small*, vol. 14, no. 45, pp. 1–11, 2018.

[59] W. Zhou, J. Chen, Z. Yang, J. Liu, and F. Ouyang, “Geometry and electronic structure of monolayer, bilayer, and multilayer Janus WSSe,” *Phys. Rev. B*, vol. 99, no. 7, pp. 1–7, 2019.

[60] C. Xia, W. Xiong, J. Du, T. Wang, Y. Peng, and J. Li, “Universality of electronic characteristics and photocatalyst applications in the two-dimensional Janus transition metal dichalcogenides,” *Phys. Rev. B*, vol. 98, no. 16, pp. 1–8, 2018.

[61] K. Ishizaka *et al.*, “Giant Rashba-type spin splitting in bulk BiTeI,” *Nat. Mater.*, vol. 10, p. 521, Jun. 2011.

[62] Q. Liu, Y. Guo, and A. J. Freeman, “Tunable Rashba Effect in Two-Dimensional LaOBiS2 Films: Ultrathin Candidates for Spin Field Effect Transistors,” *Nano Lett.*, vol. 13, no. 11, pp. 5264–5270, Nov. 2013.

[63] Y. Guo, S. Zhou, Y. Bai, and J. Zhao, “Enhanced piezoelectric effect in Janus group-III chalcogenide monolayers,” *Appl. Phys. Lett.*, vol. 110, no. 16, 2017.

[64] L. Dong, J. Lou, and V. B. Shenoy, “Large In-Plane and Vertical Piezoelectricity in Janus Transition Metal Dichalchogenides,” *ACS Nano*, vol. 11, no. 8, pp. 8242–8248, 2017.

[65] A. Y. Lu *et al.*, “Janus monolayers of transition metal dichalcogenides,” *Nat. Nanotechnol.*, vol. 12, no. 8, pp. 744–749, 2017.

[66] J. Zhang *et al.*, “Janus Monolayer Transition-Metal Dichalcogenides,” *ACS Nano*, vol. 11, no. 8, pp. 8192–8198, 2017.

[67] Wang, Qing Hua, et al. "Electronics and optoelectronics of two-dimensional transition metal dichalcogenides." Nature nanotechnology 7.11 (2012): 699

[68] Andrea Pisoni, et al. “The Role of Transport Agents in MoS2 Single Crystals.” J. Phys. Chem. C 2015, 119, 3918–3922

[69] R. E. Peierls, Ann. Inst. Henri Poincare, 1935, 5, 177–222

[70] Fan Lei, et al. “Simulation of a large size inductively coupled plasma generator and comparison with experimental data” AIP Advances 8, 015003 (2018)

[71] V A Godyak, R B Piejak and B M Alexandrovich, “Electron energy distribution function measurements and plasma parameters in inductively coupled argon plasma.” Plasma Sources Sci. Technol. 11 (2002) 525–543

[72] H Sugai, et al. “Electron energy distribution functions and the influence on fluorocarbon plasma chemistry.” H Sugai et al 2001 Plasma Sources Sci. Technol. 10 378

[73] C. Ataca, H. Ṣahin, and S. Ciraci, “Stable, Single-Layer MX2 Transition-Metal Oxides and Dichalcogenides in a Honeycomb-Like Structure.” J. Phys. Chem. C 2012, 116, 8983–8999

[74] Jun Kang, Sefaattin Tongay, Jian Zhou, Jingbo Li, and Junqiao Wu, “Band offsets

and heterostructures of twodimensional semiconductors." Appl. Phys. Lett. 102, 012111 (2013)

[75] Hyo-Chang Lee: "Review of inductively coupled plasmas: Nano-applications and bistable hysteresis physics" Appl. Phys. Rev. **5**, 011108 (2018)

[76] Hyungjin Kim, et al. "Synthetic WSe2 monolayers with high photoluminescence quantum yield." Kim et al., Sci. Adv. 2019

[77] Sefaattin Tongay et al., "Defects activated photoluminescence in two-dimensional semiconductors: interplay between bound, charged, and free excitons." SCIENTIFIC REPORTS | 3: 2657 | DOI: 10.1038/srep02657

[78] Dahyun Nam, Jae-Ung Lee & Hyeonsik Cheong, "Excitation energy dependent Raman spectrum of MoSe2." Scientific Reports | 5:17113 | DOI: 10.1038/srep17113

[79] Hulian Wang et. al, "Revealing the microscopic CVD growth mechanism of $MoSe_2$ and the role of hydrogen gas during the growth procedure." Nanotechnology 29 (2018) 314001

[80] A. Kandemir a and H. Sahin, "Bilayers of Janus WSSe: monitoring the stacking type via the vibrational spectrum." Phys. Chem. Chem. Phys., 2018, 20, 17380—17386

[81] Y.P. Varshni, "Temperature dependence of the energy gap in semiconductors." Physicia. 34 (1): 149-154. (1967)